Silicon-on-Insulator Microring Resonator Based Filters with Bent Couplers

by

Nourhan Eid

B.A.Sc, The University of Ottawa, 2014

A THESIS SUBMITTED IN PARTIAL FULFILLMENT OF THE REQUIREMENTS FOR THE DEGREE OF

Master of Applied Science

in

THE FACULTY OF GRADUATE AND POSTDOCTORAL STUDIES

(Electrical and Computer Engineering)

The University of British Columbia
(Vancouver)

October 2016

© Nourhan Eid, 2016

Abstract

In this thesis, we present and study the use of bent couplers in silicon-on-insulator (SOI) microring resonator (MRR) based filters. MRR based filters are attractive candidates in wavelength division-multiplexing (WDM) transceivers because of their compactness and low power consumptions. However, they suffer from drawbacks that include a limited free spectral range (FSR) which limit the number of channels that can be simultaneously multiplexed and/or demultiplexed. Our work investigates SOI single-ring MRR filters with bent couplers that have extended FSRs, enhanced filter performance (such as bandwidth, out-of-band rejection ratio, side-mode suppression, extinction ratio, and insertion loss) while maintaining compact footprints. Our aim is to make these filters attractive candidates to the current state-of-the-art WDM transceivers.

We first demonstrated a 2.75 µm radius MRR filter that employs bent directional couplers in its coupling regions. This MRR filter was fabricated using a 248 nm photolithography process. Our filter has a 33.4 nm FSR and a 3-dB bandwidth of 25 GHz. Also, our MRR achieved an out-of-band-rejection ratio of 42 dB, an extinction ratio of 19 dB, and a drop-port insertion loss that is less than 1 dB. Lastly, our MRR filter has a tuning efficiency of 12 mW/FSR. Then, we theoretically and experimentally demonstrated an MRR filter with bent contra-directional couplers that exhibits an FSR-free response, at both the drop and through ports, while achieving a compact footprint. Also, using bent contra-directional couplers in the coupling regions of MRRs allows us to achieve larger side-mode suppressions than MRRs with straight CDCs. The fabricated MRR filter has a minimum

suppression ratio of more than 15 dB, a 3dB-bandwidth of $\sim$23 GHz, a through-port extinction ratio of $\sim$18 dB, and a drop-port insertion loss of $\sim$1 dB. High-speed data transmission through the MRR filter is demonstrated at data rates of 12.5 Gbps, 20 Gbps, and 28 Gbps.

Preface

This thesis is based on two publications on which I am the main author. The content of Chapter 2 is based on the following publication, which has been accepted, [1]:

1. N. Eid, H. Jayatilleka, M. Caverley, S. Shekhar, L. Chrostowski, and N. A. F. Jaeger, "Wide FSR silicon-on-insulator microring resonator with bent couplers," in *IEEE 12th International Conference on Group IV Photonics*, 2015. ©2015 IEEE. Material including text and figures used with permission.

H. Jayatilleka and I conceived the idea. H. Jayatilleka created the mask layout. I did the design and simulations for the device, and performed the measurements for the fabricated device and the data analysis. M. Caverley helped me in performing the parameter extraction for the fabricated device. L. Chrostowski provided access to the fabrication technology used. I wrote the first draft of the manuscript, and N. A. F. Jaeger and M. Caverley worked with me to determine the final content and to edit the manuscript. S. Shekhar, L. Chrostowski, and N. A. F. Jaeger provided insights during the design process and S. Shekhar and L. Chrostowski feedback on the manuscript.

The content of Chapter 3 is based on the following publication which has been accepted:

2. N. Eid, R. Boeck, H. Jayatilleka, L. Chrostowski, W. Shi, and N. A. F. Jaeger, "A Silicon-on-Insulator Microring Resonator Filter with Bent Contradirectional Couplers," in *IEEE Photonics Conference*, 2016. ©2016 IEEE. Material including text and figures used with permission.

N. A. F. Jaeger and W. Shi conceived the idea. R. Boeck provided guidance and insights at the early stages of the design process. L. Chrostowski obtained access to the fabrication used in this project. I designed and simulated the device, and created the mask layout of the device. I also did measurements on the fabricated device and the data analysis. H. Jayatilleka created the setup for the high-speed testing. I wrote the first draft of the manuscript and N. A. F. Jaeger worked with me to determine the technical content and to revise and edit the manuscript. All the co-authors provided feedback on the manuscript.

Also, the content Chapter 3 is mainly based on the following publication which has been submitted to a journal:

3. N. Eid, R. Boeck, H. Jayatilleka, L. Chrostowski, W. Shi, and N. A. F. Jaeger, "FSR-Free Silicon-on-Insulator Microring Resonator Based Filter with Bent Contra-Directional Couplers," [submitted in 2016].

N. A. F. Jaeger and W. Shi conceived the idea. R. Boeck provided guidance and insights at the early stages of the design process. L. Chrostowski obtained access to the fabrication used in this project. I designed and simulated the device, and created the mask layout of the device. I also did measurements on the fabricated device and the data analysis. H. Jayatilleka created the setup for the high-speed testing. I wrote the first draft of the manuscript and N. A. F. Jaeger worked with me to determine the technical content and to help in writing the final version of the manuscript. All the co-authors provided feedback on the manuscript.

Table of Contents

List of Tables

List of Figures

List of Acronyms

SOI	silicon-on-insulator
PIC	photonic integrated circuit
WDM	wavelength-division multiplexing
DWDM	dense WDM
DWDM	dense wavelength-division multiplexing
SFP	small form-factor pluggable
QSFP	quad small form-factor pluggable
CFP	C form-factor pluggable
MUX	multiplexer
DEMUX	demultiplexer
OADM	optical add-drop multiplexer
FSR	free spectral range
AWG	arrayed waveguide grating
MZI	Mach-Zehnder interferometer
MRR	microring resonator

CDC	contra-directional coupler
PD	photodetector
MZM	Mach-Zehnder modulator
GC	grating coupler
3dB-BW	3dB-bandwidth
ER	extinction ratio
OBRR	out-of-band rejection ratio
SMSR	side-mode suppression ratio
BER	bit error rate
BERT	bit error rate tester
VOA	variable optical attenuator
PPG	pulse pattern generator
EDFA	erbium-doped fiber amplifier
OTF	optical tunable filter
DCA	digital communication analyzer
TLS	tunable laser source

Acknowledgments

I would like to begin by expressing my profound gratitude to my parents and to my spouse for providing me with the support and continuous encouragement throughout my studies

I also express my sincere gratitude to my supervisor Dr. Nicolas A. F. Jaeger for the guidance and mentorship that he has provided me. I am especially grateful for his continuous support and patience during my studies. I would also like to thank Dr. Lukas Chrostowski for all the opportunities and useful feedback that has assisted me during this work.

I would also like to thank all my colleagues, that I have worked with, for their help and collaboration, and especially Hasitha Jayatilleka, Robert Boeck, Michael Caverley, Han Yun, Kyle Murray and Minglei Ma.

I acknowledge Ranovus Inc. for providing an internship opportunity during my studies. I also acknowledge CMC Microsystems for the provision of services that facilitated this research as well as Lumerical Solutions, Inc., and Mentor Graphics, Corp., for the design tools. Additionally, I acknowledge the Natural Sciences and Engineering Research Council of Canada as well as the SiEPIC program for financial support. Part of this work was conducted at the University of Washington Nanofabrication Facility, a member of the NSF National Nanotechnology Infrastructure Network..

Chapter 1

Introduction

1.1 Silicon Photonics

Silicon-on-insulator (SOI) is an attractive platform for photonic integrated circuits (PICs) used in telecommunication applications as well as in high-performance computing systems [2, 3]. Thus, tremendous research efforts have been targeted toward silicon photonics by the research community in academia and industry. An advantage of SOI is that on it devices can be fabricated using complementary metal-oxide-semiconductor (CMOS) compatible processes which are mature and reliable, are low cost, and allow for monolithic integration of the photonics devices with the electrical circuits [4]. In addition, the high refractive index contrast between the silicon waveguides and the oxide cladding allow for the creation of compact devices and small waveguide bends. This facilitates dense integration of the optical components in order to realize photonic chips with small footprints. There are numerous optical components that are demonstrated on SOI platforms, such as detectors [5, 6], modulators [7], filters [8], edge couplers [9], grating couplers [10], and polarization splitters-rotators [11].

1.2 WDM Systems and Transceivers

Wavelength-division multiplexing (WDM) is widely used in the optical interconnects of data centers and high-performance computing systems [12–15]. In WDM systems, multiple channels of optical signals (each channel having a different center wavelength) are simultaneously transmitted over the same fiber. As a result, WDM systems provide means for increasing the aggregate bandwidths of the optical links; namely, if a WDM system has N channels and each channel transmits at data rate R, then the aggregate data rate of the link is NxR. In fact, some WDM based links can transmit several terabits per second [16, 17]. WDM systems can either be coarse WDM (CWDM) systems, which can transmit up to 16 channels per fiber, or dense WDM (DWDM) systems, where channels are more closely spaced and can transmit up to 80 channels per fiber (at a 50 GHz channel spacing) [18]. While, DWDM based links can transmit a larger number of channels per fiber and have higher aggregate bandwidths than CWDM links, each of the channels in a CWDM system has a wider bandwidth and a flat-top response. Thus, CWDM systems have more tolerance to laser wavelength drift [19]. As a result, CWDM systems are used in short-range communications as stable laser sources (which are expensive) are not required, and hence such systems are more cost-effective. On the other hand, DWDM systems are predominantly used in long-haul communications. This is because in long-haul communications, it is more desirable to transmit a large number of channels in a single fiber, as well as the costs associated with having stable laser sources can be tolerated in long-haul communications.

WDM transceivers are important components for optical interconnects. Figure 1.1 shows the block diagram of a typical architecture of a four-channel WDM transceiver. At the transmitter end, various lasers, each having a unique wavelength, are modulated by the input data; the most common implementations of the modulators include Mach-Zehnder modulators [20, 21], electro-absorption modulators [22, 23], and microring modulators [24–27]. The modulated optical signals are then multiplexed into the fiber channel via a multiplexer (MUX) that is made

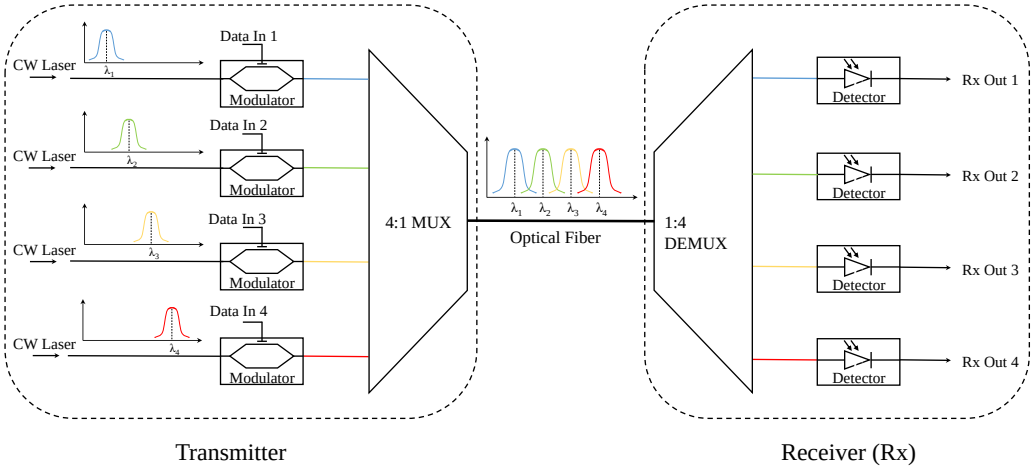

Figure 1.1: A block diagram of a WDM transceiver, which is composed of a four-channel transmitter and a four-channel receiver. The block diagram shows the optical components of the transceiver, but not the electrical components.

from several optical add-drop multiplexers (OADMs). At the receiver end, the optical signals are demultiplexed via a demultiplexer (DEMUX), also made from several OADMs. The de-multiplexed optical signals are then converted to electrical signals via photodetectors (PDs). Such detectors can be Germanium PIN photodetectors [28] or avalanche photodiodes [29].

Several companies are developing WDM transceivers that use the SOI platform for optical interconnects. Intel, for instance, demonstrated a 40 Gbps silicon photonics CWDM link; the link is made of four channels and each channel carries a data rate of 10 Gbps (4 x 10 Gbps) [30]. Luxtera has also developed a 4 x 10 Gbps monolithically integrated transceiver [31], and has recently announced its 4 x 26 Gbps transceiver for data centers [32]. In addition, IBM has demonstrated its fully integrated silicon photonics chip for 100 Gbps WDM transceivers [33]. Skorpios Technologies has demonstrated a 100 Gbps WDM transceiver that uses an SOI platform [34]. Lastly, Inphi and M/A-COM have each recently announced their silicon photonics transceiver chips for 100G WDM data center applications [35, 36]. A large number of the WDM transceivers developed commercially are

small form-factor pluggable (SFP) transceivers. There are two common types of SFP transceivers: quad small form-factor pluggable (QSFP) transceivers, which support four WDM channels and speeds up to 100 Gbps [37], and C form-factor pluggable (CFP) transceivers, which support 40G and 100G Ethernet [38]. Hence, there is a trend toward developing compact and pluggable transceiver modules that can support high-speed data signals of up to 100 Gbps and 400 Gbps [39]. QSFP28 transceivers, which are QSFP transceivers that support four channels each with data rates of 28 Gbps, are an example of the demand to increase the aggregate bandwidths supported by WDM transceivers, by increasing the number of transmit channels, while maintaining the small footprints of SFP chips [40]. The transceivers discussed above that are offered by Luxtera, Skorpios Technologies, Inphi, and M/A-COM are QSFP28 transceivers.

1.3 Filters in WDM Links

Filters are important building blocks of WDM transceivers where they are used as OADMs on both the transmitter and receiver sides. There are some design parameters that a proposed filter design should have in order to be used in commercial WDM transceivers [41, 42]. One of the design requirements is that a WDM filter should have a compact footprint so that it can be used in SFP transceiver chips. This design requirement becomes especially important in QSFP transceivers where the circuits of these transceivers can have up to four filters (for the four transmit channels), and these circuits should be within the space requirements of SFP chips. As a result, it is important to keep these filters as compact as possible and densely integrate the components of SFP transceivers. Another filter design requirement is that a transceiver should have a large channel capacity, and accordingly a filter should have a wide free spectral range (FSR) to increase the number of channels that can be MUXed/DEMUXed in a particular band. Furthermore, a filter should have a wide bandwidth per channel which contributes to increasing the aggregate bandwidth of the link. For instance, the filters used in QSFP28 transceivers should have bandwidths that support at least 28 Gbps. Additionally,

a filter is required to have good thermal efficiency to reduce the amount of power required to tune the center wavelengths. Additionally, a filter should have low channel cross-talk [43], have low insertion loss, have a tolerance to fabrication errors and temperature changes, and be fully reconfigurable (for instance in bandwidth [44]) .

1.3.1 Common Types of WDM Filter

Some of the most common types of filter used in WDM transceivers include echelle gratings [45], arrayed waveguide gratings (AWGs) [46], Mach-Zehnder interferometer (MZI) lattices [47], and contra-directional couplers (CDCs) [48]. In this section, we will describe the principle of operation of each of these filters and present some of their strengths and weaknesses.

1.3.1.1 Echelle gratings

A schematic of an echelle grating filter is shown in Figure 1.2. In echelle grating filters, when used as DEMUXs, light from the input waveguide enters the free propagation region where it diverges and propagates to the diffraction grating. The etched facets (teeth) of the diffraction grating cause the light to diffract at angles which are wavelength dependent. Also, the angle of diffraction at each incident wavelength depends on where on the grating it impinges. The diffracted light is focused onto a series of output waveguides bu the grating, such that the light focused on each of the waveguides has a unique wavelength. This operation is reversed when echelle grating filters are used as MUXs. Because the designs of echelle gratings require careful placement of the input and output waveguides, the filter performance is sensitive to fabrication errors [49]. Furthermore, echelle grating filters occupy relatively large footprints and have relatively large insertion losses.

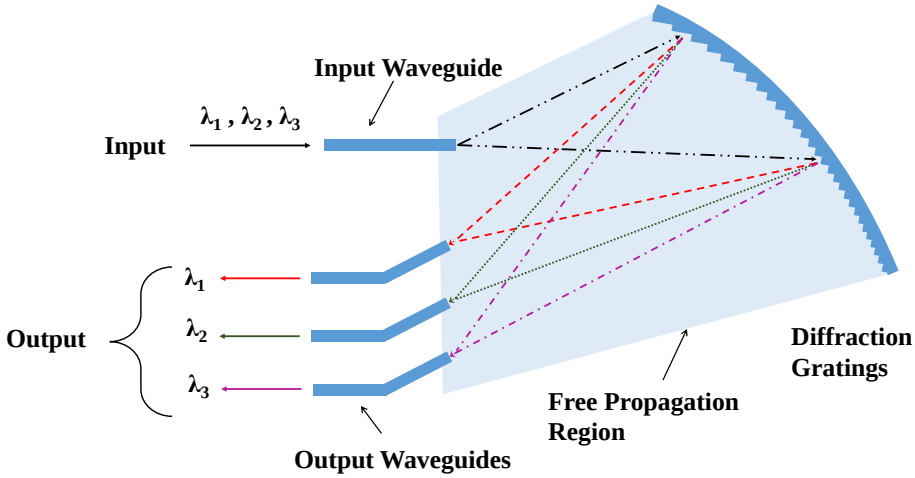

Figure 1.2: A schematic of an echelle gratings filter that is used as a DEMUX.

1.3.1.2 Arrayed Waveguide Gratings (AWGs)

A schematic of an AWG is shown in Figure 1.3. The AWG is similar in principle to the echelle grating. In AWGs, when used as DEMUXs, the input light is split, via a coupler (such as a star coupler), into multiple paths which then propagate through an array of waveguides. Each waveguide has a constant increment (plus or minus) in length with respect to its adjacent waveguides. The linearly increasing lengths of the array of waveguides cause linearly varying phase shifts at the outputs across the waveguides. These phase shifts are wavelength-dependent such that the wavefront for a particular wavelength, at the end of the waveguide array, is tilted at a certain angle such that the light is directed towards a particular output waveguide. As a result, the light propagating in each of the output waveguides will have a unique wavelength.

AWG filters occupy relatively large footprints and have large insertion losses. However, in an AWG, its design can allow for independently tuning each of the waveguides to control the wavelengths of each of the output channels, which is not possible in echelle grating filters. However, the different waveguides are prone to thermal crosstalk.

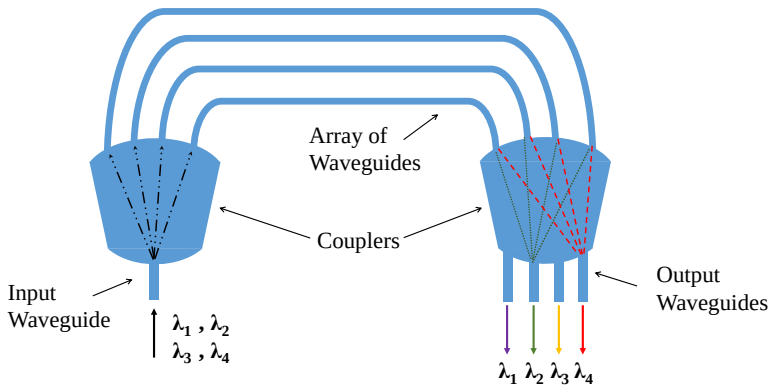

Figure 1.3: A schematic of an AWG filter that is used as a DEMUX.

1.3.1.3 MZI Lattices

An MZI lattice filter is made from multiple cascaded stages of unbalanced MZIs as shown in the schematic in Figure 1.4. In an unbalanced MZI, one of the arms of the MZI has a different length with respect to the other arm; this causes constructive interference at certain wavelengths, at the output, because of the wavelength-dependent phase delay. As a result, such an MZI will have a sinusoidal response with peaks at equally spaced wavelengths. In this filter, a series of cascaded unbalanced MZIs are used so that each of the stages filters out some of the wavelength peaks and passes the remaining wavelengths, see Figure 1.4. Accordingly, the resulting output response of this filter will have a single wavelength peak at a particular band.

In order to use such a filter as a MUX/DEMUX, the first MZI stage should be branched into a tree of MZIs, each of the branches selecting a unique wavelength. As apposed to echelle gratings and AWG filters, MZI lattice filters can achieve lower insertion losses. However, active tuning is required to align all of the MZI stages, which increases the power consumed by the filter. Also, MZI lattice filters (especially when used as a MUX/DEMUX) can have large footprints.

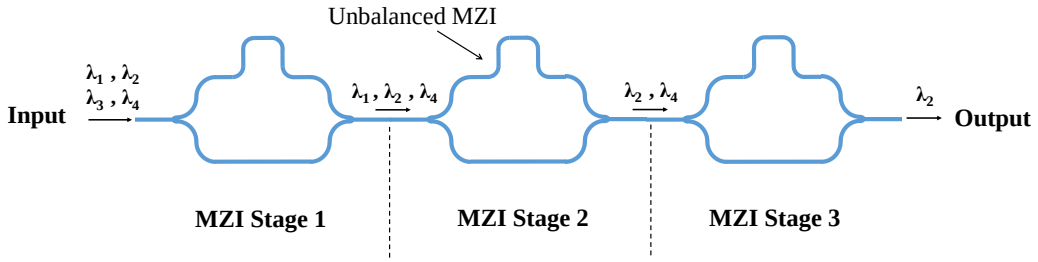

Figure 1.4: A schematic of an MZI lattice filter.

1.3.1.4 Contra-directional couplers (CDCs)

CDCs are another type of add-drop filter that can be used in WDM based links [48]. The contra-directional coupling occurs due to the corrugations (gratings) on the inner sidewalls of the waveguides which cause coupling between the forward propagating mode of one waveguide and the backward propagating mode of the other waveguide (see Figure 1.5) [50]. The contra-directional coupling occurs at the wavelength at which the phase-match condition is satisfied, and thus they are used as filters. CDCs have flat-top responses with wide bandwidths, that can exceed 3 nm. These wide bandwidths allow for error-free transmission within a range of operating temperature drift of the laser and the filter, and thus CDCs have higher temperature tolerance than other types of filters. Nevertheless, CDCs are not appropriate for DWDM systems, where a spacing as low as 50 GHz is required. This is because a CDC, with a typical coupling length, will have a bandwidth that exceeds a typical DWDM channel spacing (50 GHz to 200 GHz). Moreover, CDCs have feature sizes that are small and comparable, or less than, photolithography wavelengths (193 nm or 248 nm). This makes it difficult to fabricate CDCs using conventional optical lithography processes. In other words, the gratings in the walls of a CDC, fabricated using optical lithography, will be smoothed by the lithography and fabrication errors are more likely to occur.

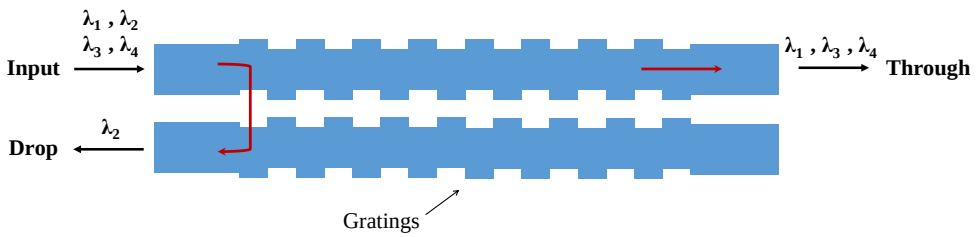

Figure 1.5: A schematic of a CDC coupler that is used as a filter.

1.3.2 MRR Based Filters

Silicon microring resonator (MRR) based filters are attractive candidates in WDM transceivers because of their compact sizes and low power consumptions [17]. On the other hand, due to the relatively high sensitivity of MRRs, wavelength stabilization is typically needed to offset the effect of fabrication errors and changes in the external environment on the resonant wavelengths of MRRs. Although, there are several stabilization techniques that have been demonstrated, especially for single-ring MRRs [51], MRR stabilization, in general, is a disadvantage for MRRs as power is needed to stabilize them.

In addition, MRRs have limited FSRs which limits the number of transmit channels in a particular band, and hence the aggregate bandwidth of the link. As a result, several MRR designs have been demonstrated that extended the MRR's FSR [41]. One technique uses the Vernier effect in which multiple series-coupled MRRs are used to extend the FSR [52]. Another method proposed is to use two-point coupling to an MRR in which an MZI is used as the coupler to act as a filter to the MRR side modes [53]. Although the previously mentioned techniques have been effective in increasing the MRRs' FSRs and in demonstrating MRR filters with improved performance (in some cases the demonstrated filters met the DWDM commercial specifications [54]), they have complex designs. As a result, designing the MRRs that use these techniques is relatively complicated and stabilizing them using automatic control algorithms can be difficult. Also, these designs were not compact and required tuning several MRRs which increased the power consumption of the filter. In conclusion, because of some of the aforemen-

tioned drawbacks of MRR filters, they are not widely used in commercial WDM transceivers. Accordingly, more research effort needs to be invested to improve the designs of MRR filters and mitigate their weaknesses.

1.4 Thesis Objective

The goal of the research presented in this thesis is to design MRR based filters and solve some of the weaknesses discussed above (in section 1.3.2). This work is aimed at making MRRs more appealing as filters in commercial WDM transceivers. Specifically, we used bent couplers in our MRR filters to improve their designs. One of our objectives is to use single-ring MRR filters, with extended FSRs, as they can be more compact and energy-efficient solutions as compared to multiple-coupled MRR filters. Thus, we proposed a wide FSR, single-ring MRR filter with bent directional couplers. Bent directional couplers allow for fabrication of small radii MRRs using 248 nm optical lithography, while achieving wide FSRs and enhanced performance. Thus, our demonstrated MRR filter with bent couplers has an FSR of $\sim$ 34 nm and also has sufficient coupling coefficient to achieve a wide 3dB-bandwidth (3dB-BW) of 25 GHz and an out-of-band rejection ratio (OBRR) of 42 dB. Such results were previously difficult to achieve using MRRs fabricated using typical optical lithography processes.

CDCs are another kind of coupler that are used to extend the FSRs of single-ring MRR filters. Since CDCs are wavelength selective couplers, they have been used in the coupling regions of MRRs to eliminate the FSRs (within the wavelength range over which silicon is transparent) [55]. Thus, an ”FSR-free” response can be achieved using MRR filters consisting of a single ring. In this thesis, we propose and demonstrate an MRR filter that uses bent CDCs in the coupling regions, instead of straight CDCs, and thus obtain a more compact filter as compared to a previously demonstrated single-ring MRR filter that used straight CDCs (three-fold decrease in the filter's footprint) [55]. Also, our design achieves improved performance and side-mode suppression as compared to the previously demonstrated filter [55].

1.5 Thesis Overview

This thesis is divided into four chapters. In this chapter, we give a brief introduction to silicon photonics, as well as an overview of WDM systems and transceivers. Then, we discuss the various kinds of filter used in WDM transceivers as well as the current challenges in using MRR based filters in current commercial WDM transceivers. Also, various implementations of MRR filters are presented and the thesis objective is outlined. In the next two chapters, we present and experimentally demonstrate, two kinds of MRR based filter that use bent couplers in their coupling regions. Chapter 2 presents an MRR filter with bent directional couplers that is compact, has a wide FSR, and a wide bandwidth. Chapter 3 presents an MRR filter with bent CDCs that is more compact than a previously demonstrated MRR filter with straight CDCs, has an FSR free response at both the drop port and the through port, has a relatively large side-mode suppression, and has a wide bandwidth. Finally, in Chapter 4, a summary of the thesis, as well as conclusions and suggestions for future work are provided.

Chapter 2

Wide FSR Silicon-on-Insulator Microring Resonator Filter with Bent Directional Couplers

MRR based filters are attractive for use in PICs due to their compact footprints. In applications such as WDM, a wide FSR, that is greater than the C-band, is desirable in order to add or drop only a single channel in the band. As a consequence, many SOI MRR based designs have been proposed and demonstrated to achieve this goal, such as using MRRs with two-point coupling [53] or the Vernier effect [56]. However, these schemes use mutually coupled rings, which require tuning of the resonance wavelength of each ring. Alternatively, single-ring MRRs are attractive because they have smaller footprints and there are techniques available for stabilizing their resonance wavelengths [51, 57]. Hence, significant effort has gone into creating MRRs with radii below 3 μm in order to widen their FSRs [58–60]. Such small radius MRRs are typically point coupled [58–60]. When using point coupled MRRs, small gaps are usually used to achieve the coupling needed to obtain wide bandwidths. These small gaps have usually been realized on SOI using electron-beam lithography.

Here, in this chapter, using bent directional couplers, that are wrapped around

a portion of the ring, [61, 62] are explored. By using bent directional couplers, the MRR's coupling coefficient can be increased because the couplers have longer coupling lengths and, therefore, allowing the use of coupler gaps large enough for fabrication using optical lithography. Optical lithography is preferable over electron-beam lithography because it is low cost and it allows for mass production of PICs. The MRRs presented here are also designed with optimal phase-matching in the couplers to maximize the MRRs' coupling coefficients and to increase their bandwidths. We will describe below (in section 2.1) how to achieve the optimal phase-matching in bent directional couplers, as well as give a brief introduction to bent directional couplers. Also, we will derive (in section 2.2) the equations used to optimize an MRR design for a target 3dB-BW, OBRR, IL_{drop}, and extinction ratio (ER). Last but not least, we will describe the design procedure and present experimental results for an MRR using bent couplers that has a 2.75 µm radius, a 33.4 nm FSR, and a 3dB-BW of 25 GHz.

2.1 Bent Directional Couplers

Bent directional couplers are made of two waveguides in which one of the waveguides, the bus waveguide in this case, is partially curved around another waveguide, the ring waveguide, as shown in Figure 2.1. Bent couplers have been previously demonstrated to be more broadband (less wavelength sensitive) and to be more reliable and tolerant to fabrication errors than conventional directional couplers [63]. Thus, they have been used as broadband 50/50 splitters (or couplers) [64], as well having been proposed as short, broadband polarization splitters [65, 66]. Additionally, 50/50 splitters based on bent couplers have been used in MZIs to form compact, low insertion loss, high extinction ratio MZI switches [67]. Bent couplers were also used in the coupling regions of all-pass MRRs [62] and fourth-order (i.e., using four series-coupled MRRs) MRR filters [61] to increase the coupling coefficients of these MRRs. Although these bent couplers were proposed as broadband couplers, we intend to use them in our MRR filters for the purpose of increasing their couplings and not to make use of their broad-

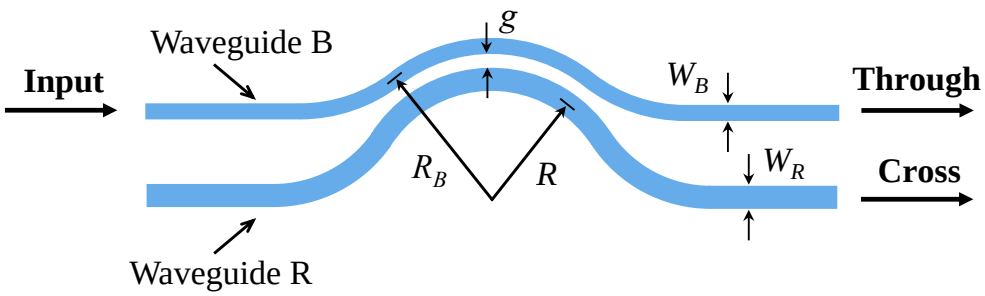

Figure 2.1: A schematic of a bent directional coupler.

band operation.

In a bent directional coupler, the bend radius of the bus waveguide is different than the bend radius of the ring waveguide. Thus, the ring and bus waveguides have different coupling lengths. In the case that the ring and bus waveguides are identical (i.e., have the same widths and propagation constants), the local normal modes of the bus and ring waveguides at any point along the coupler will have different phases and will not be phase-matched. Here, we assume that each of the waveguides will support one local normal mode and that the waveguides are isolated. As a result, a full exchange of power between the waveguides (when used in a bent coupler) will not be possible and the cross coupling coefficients will be lower than what could be achieved in conventional directional couplers. Hence, in order to optimize the coupling coefficients in bent couplers, the bus and ring waveguides should be asymmetric (i.e., have different widths) so that the phase-match condition is satisfied; the phase-match condition is given by

$$n_B R_B = n_R R \tag{2.1}$$

where n_B and n_R are the effective indices of the fundamental local normal modes in the bus waveguide (waveguide B) and the ring waveguide (waveguide R), respectively. R is the bend radius of waveguide R, and R_B is the bend radius of

waveguide B and is given by

$$R_B = R + \frac{W_R}{2} + g + \frac{W_B}{2} \tag{2.2}$$

where W_R and W_B are the widths of waveguides R and B, respectively, and g is the coupler's gap width. Here, n_B and n_R depend on W_B and W_R. Accordingly, to design a bent coupler, our desired values for R, W_R, and g are first chosen. W_B is then designed to satisfy the phase-match condition for these chosen values. This is done by plotting $n_B R_B$ at various values of W_B, and choosing W_B at the point at which our curve intersects our $n_R R$ value; this is illustrated in Figure 2.2(a). Here, R = 5 µm, W_R = 500 nm, and g = 200 nm and, according to the plot, W_B is 380.8 nm (at the point $n_B R_B = n_R R$ = 12.2 µm). In order to verify the phase-match condition, the demonstrated bent coupler is simulated in Lumerical FDTD Solutions by Lumerical Solutions, Inc. Here, the bent coupler is simulated at various values of W_B (including W_B = 380.8 nm), and the resulting cross power coupling coefficient, $|\kappa|^2$, is plotted for these W_B values as shown in Figure 2.2(b). In the plot, the maximum $|\kappa|^2$ value occurs at W_B = 380.8 nm, which is clearly close to the maximum attainable $|\kappa|^2$ for the simulated coupler.

2.1.1 Analysis of Bent Waveguides

Given that bent waveguides form an important part of bent couplers and MRRs, the effects of bending on the effective indicies, group indicies, and losses of bent waveguides are presented in this section. The bent waveguides are simulated at different bend radii using Lumerical MODE Solutions by Lumerical Solutions, Inc. Here, the simulated waveguides are strip waveguides with widths of 650 nm and heights of 220 nm, and are surrounded by oxide cladding. The electric field profile of the fundamental quasi-TE mode in a straight waveguide is shown in Figure 2.3(a), and the field profiles of the fundamental quasi-TE mode in bent waveguides with radii of 3 µm and 1.5 µm are shown in Figure 2.3(b) and 2.3(c), respectively. Clearly, in the straight waveguide, the mode is positioned in the

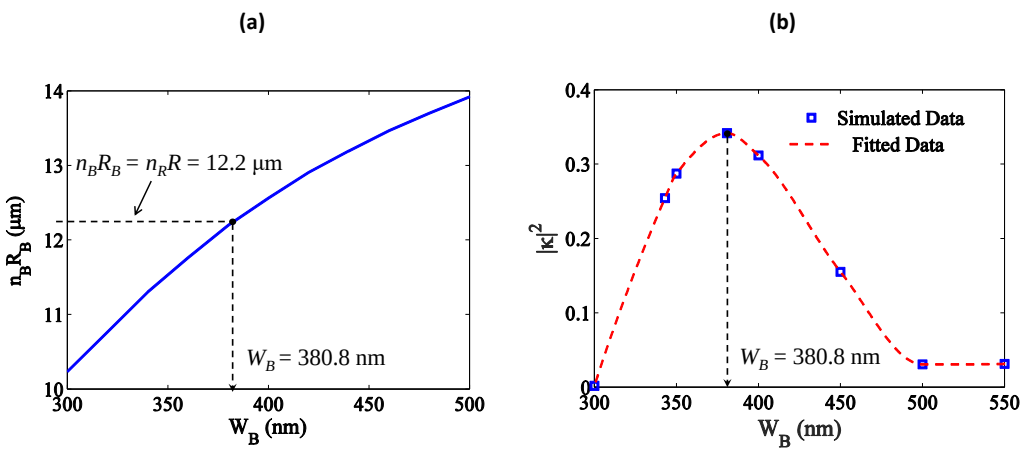

Figure 2.2: A plot of (a) $n_B R_B$ versus W_B and (b) $|\kappa|^2$ versus W_B for a bent coupler with $R = 5$ µm, $W_R = 500$ nm, and $g = 200$ nm. The plot of the fitted data in (b) is done using the shape-preserving fit in MATLAB®.

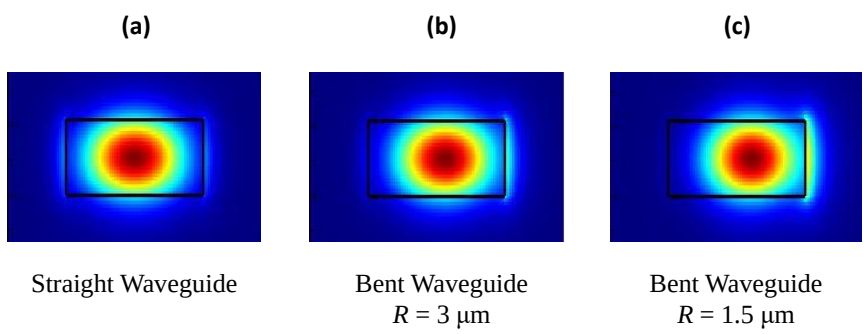

Figure 2.3: The electric field profile of the fundamental quasi-TE mode in (a) a straight waveguide, (b) a bent waveguide with a bend radius, R, of 3 µm, and (c) a bent waveguide with $R = 1.5$ µm. The waveguides have widths of 650 nm and heights of 220 nm.

waveguide such that its peak power coincides with the center of the core of the waveguide. As the waveguide is bent, the mode is displaced toward the outside of the bend; the more the waveguide is bent (i.e., the more the bend radius decreases), the more the mode is pushed toward the outside of the bend.

Moreover, the effective indicies, group indicies, and losses (commonly referred to as bending losses) are plotted at various values of bend radii, see Figure

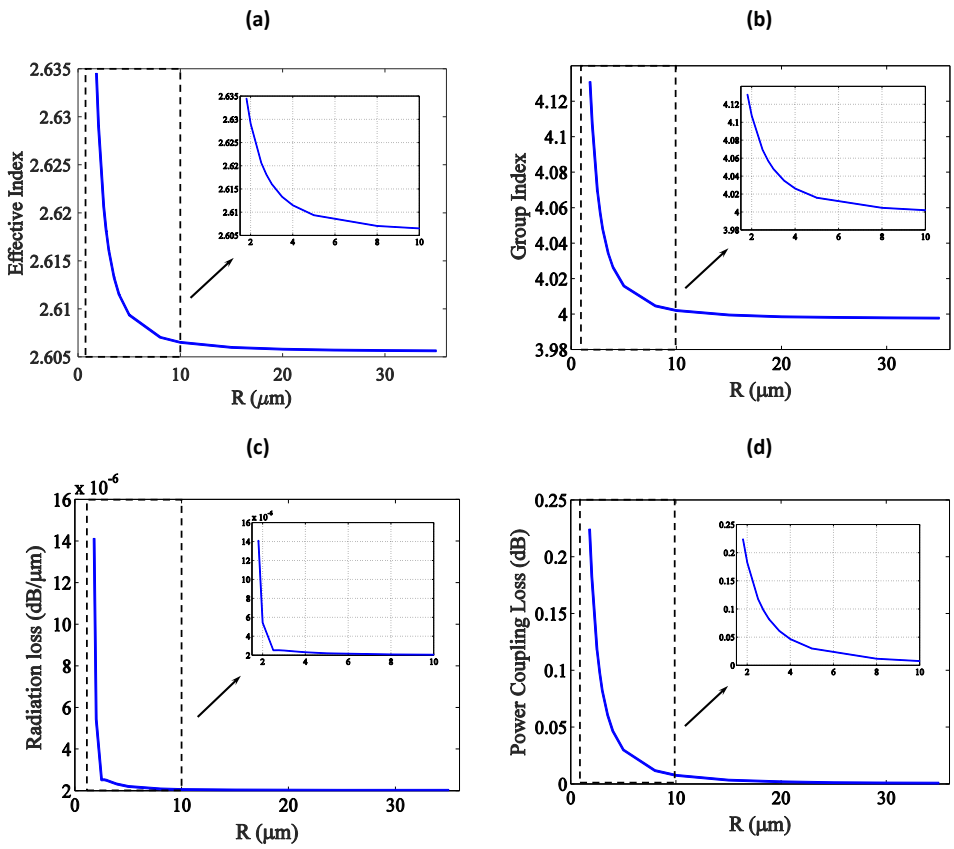

Figure 2.4: Plots of (a) the effective index, (b) the group index, (c) the radiation loss in dB/μm, and (d) the power coupling loss in dB at various values of bend radius, R.

2.4. The effective index decreases as the bend radius of the waveguide increases as shown in Figure 2.4(a). In addition, the group index decreases as the bend radius increases because of the decrease in the effective index, see Figure 2.4(b). The losses in bent waveguides are caused by the radiation losses and, predominantly, by the power coupling losses. In Figure 2.4(c), the radiation loss decreases as the bend radius increases. The power coupling loss arises from mode mismatches between the fields in the straight waveguide section and the bent waveguide section. The power coupling loss decreases as the bend radius increases as shown in

Figure 2.4(d). This is because, as the bend radius decreases, the mode is pushed further out of the waveguide, and the mode mismatch between the straight and bent waveguides increases. In the plot of coupling losses in Figure 2.4(d), there is no offset between the center of the core of the straight waveguide and the center of the core of the bent waveguide coupling losses. However, the coupling losses can be decreased by introducing the necessary offset between the center of the core of the straight waveguide and the center of the core of the bent waveguide. In conclusion, bent waveguides, typically, have larger effective indicies, group indicies, and losses than straight waveguides.

2.2 Microring Resonators

MRRs are commonly used in WDM transceivers as filters and as modulators [17, 68–71]. MRRs can be used in optical delay lines when used as coupled resonator optical waveguides (CROWs) [72], in sensing applications [73], and in external cavity lasers as reflectors [74]. MRRs are resonating devices which are formed by having a waveguide in a closed loop (i.e., forming a ring or a racetrack) that is coupled to external bus waveguides. The microrings can be coupled to the bus waveguides via directional couplers that have coupling lengths, L_c, as shown in Figure 2.5(a). The MRR shown in Figure 2.5(a) is known as a racetrack resonator. The MRR can be also be point coupled, with $L_c = 0$, as shown in Figure 2.5(b). The MRR shown in Figure 2.5(b) is a classical (round) microring resonator. At the resonant wavelengths, the optical signal in the microring undergoes an integer multiple of 2π phase change when it propagates once around the microring; this leads to the optical signal constructively interfering within the resonator and resonance occurs. As a result, there can be multiple resonant wavelengths. The resonances are evenly spaced in frequency and the spacing between them is characterized by the FSR. Here, we use the FSR as the spacing, in wavelength, between the resonances around 1550 nm and is calculated as FSR $\approx \lambda_r^2/n_g L_{rt}$, where λ_r is the resonant wavelength and n_g is the group index. The FSR is usually controlled by the roundtrip length of the MRR, L_{rt}, in which the

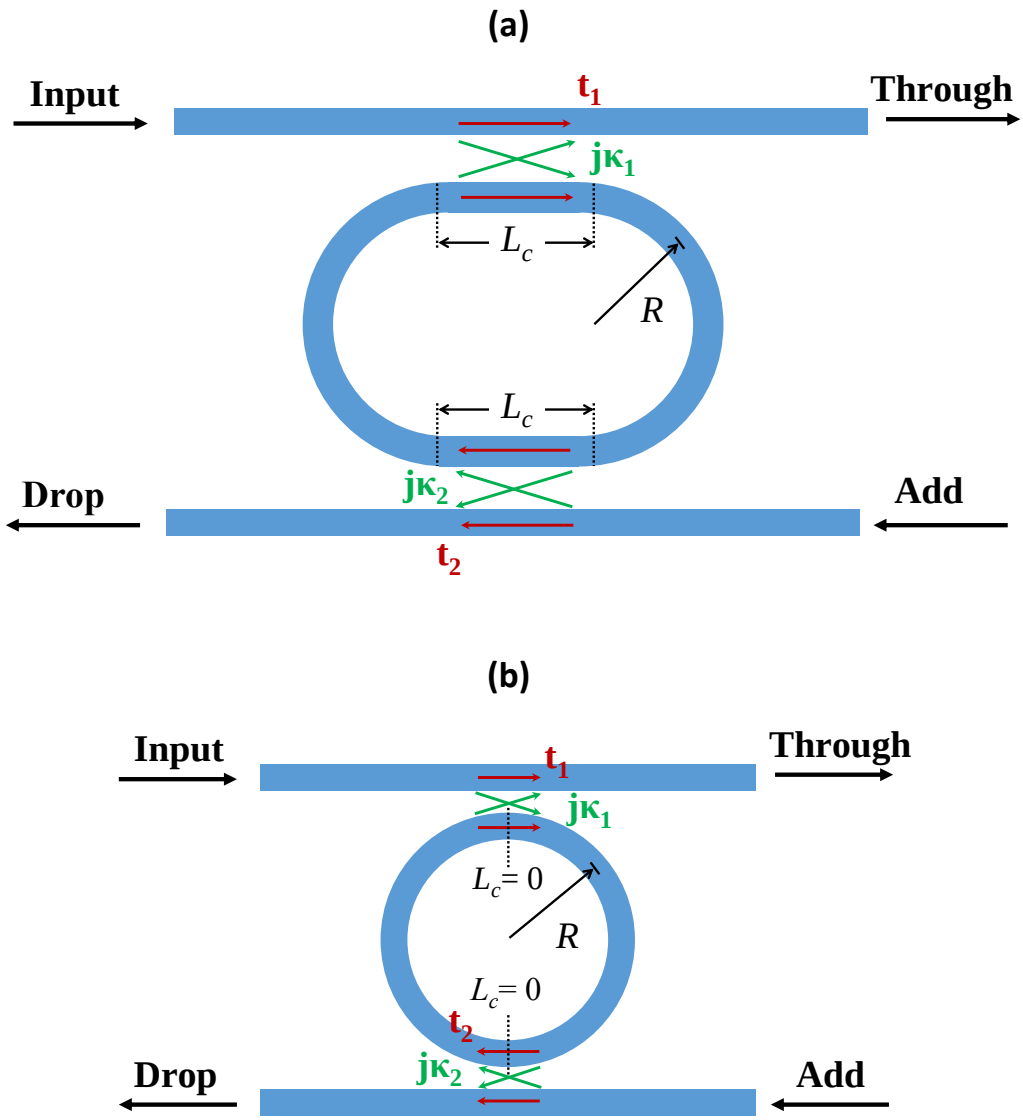

Figure 2.5: Schematics of (a) a racetrack resonator and (b) a point-coupled MRR.

FSR is inversely proportional to L_{rt}. L_{rt} is determined using R and L_c and is given as $L_{rt} = 2\pi R + 2L_c$ for racetrack resonators and as $L_{rt} = 2\pi R$ for point coupled MRRs.

Other design parameters are the couplers' gap widths between the ring and bus waveguides. These gap widths, together with L_c, control the field coupling coefficients of the couplers. These coupling coefficients are essential in defining the MRR's response and, consequently, in determining some of the filter performance parameters such as the Q-factor, the 3dB-BW, the drop-port insertion loss (IL_{drop}), the OBRR, and the ER [75]. The MRR's electric field transfer functions at the drop port, $\overline{G}_{drop}$, and the through port, $\overline{G}_{thru}$, are given by

$$\overline{G}_{drop} = \frac{-\kappa_1 \kappa_2 \sqrt{\chi}}{1 - t_1 t_2 \chi} \tag{2.3}$$

and

$$\overline{G}_{thru} = \frac{t_1 - t_2 \chi}{1 - t_1 t_2 \chi} \ , \tag{2.4}$$

respectively, where

$$\chi = a\, e^{-j\frac{2\pi n_R}{\lambda} L_{rt}} \ , \tag{2.5}$$

$$a = e^{-\frac{\alpha}{2} L_{rt}} \ , \tag{2.6}$$

and where n_R is the effective index of the ring waveguide and $\alpha/2$ is the waveguide propagation field loss in nepers per meter (i.e., α is the power loss). Also, κ_1 and κ_2 are the magnitudes of the field coupling coefficients of the couplers as illustrated in Figures 2.5(a) and 2.5(b). t_1 and t_2 are the magnitudes of the field transmission coefficients and are calculated as (assuming lossless couplers),

$$t_1 = \sqrt{1 - \kappa_1^2} \qquad \text{and} \qquad t_2 = \sqrt{1 - \kappa_2^2} \tag{2.7}$$

Here, we assume that the equations presented, in this section, apply equally to both of the MRRs in Figures 2.5(a) and 2.5(b), and that both MRRs are asymmetric add-drop MRRs. In asymmetric MRRs, the directional couplers each have

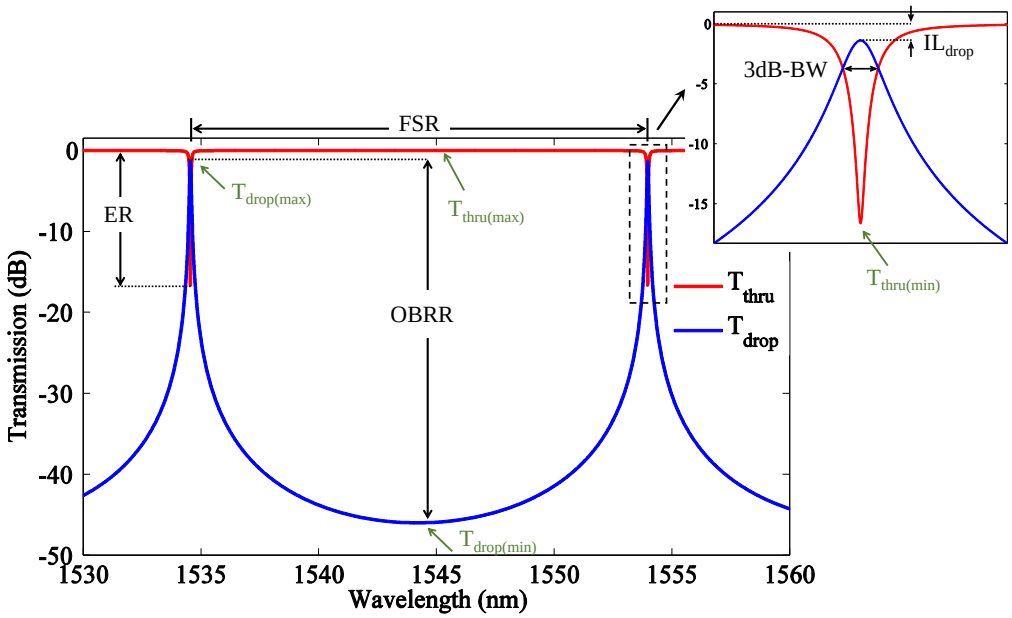

Figure 2.6: A plot showing the drop-port and through-port responses of an MRR. An inset shows zoomed-in responses around the resonant wavelength.

different gap sizes and/or the bus waveguides each have different widths. From equations 2.3 and 2.4, the magnitude-squared responses of an MRR at the drop port, T_{drop}, and at the through port, T_{thru}, are given by

$$T_{drop} = |\overline{G}_{drop}|^2 = \frac{\kappa_1^2 \kappa_2^2 a}{1 + (t_1 t_2 a)^2 - 2 t_1 t_2 a \cos(\phi_{rt})} \tag{2.8}$$

and

$$T_{thru} = |\overline{G}_{thru}|^2 = \frac{t_1^2 + (t_2 a)^2 - 2 t_1 t_2 a \cos(\phi_{rt})}{1 + (t_1 t_2 a)^2 - 2 t_1 t_2 a \cos(\phi_{rt})} \ , \tag{2.9}$$

respectively, where ϕ_{rt} is the phase change (of the electric field) after a roundtrip of the micororing and $\phi_{rt} = -\frac{2\pi n_R(\lambda_o)}{\lambda_o} L_{rt}$.

The magnitude responses, in equations 2.8 and 2.9, are then used to derive analytical equations for the IL_{drop}, the OBRR, the ER, and the 3dB-BW. The

equations that determine these parameters will be important in our MRR design procedure; as we shall see, these equations will be used in order to optimize the coupling coefficients to improve the filter performance. First, we define the peaks and minima of an MRR's drop-port response and through-port response. Namely, we derive $T_{drop(max)}$, which is the maximum power level of the drop-port response that occurs at the resonant wavelengths at ϕ_{rt}=-2πm (m = 0,1,2,...) and $T_{drop(min)}$, which is the minimum power level of the drop-port response that occurs between the resonant wavelengths at ϕ_{rt}=-2π(m$\pm$0.5). Furthermore, we derive $T_{thru(max)}$, which is the maximum power level of the through-port response that occurs between the resonant wavelengths (at ϕ_{rt}=-2π(m$\pm$0.5)) and $T_{thru(min)}$, which is the minimum power level of the through-port response that occurs at the resonant wavelengths (at ϕ_{rt}=-2πm), see Figure 2.6. Accordingly, $T_{drop(max)}$, $T_{drop(min)}$, $T_{thru(max)}$, and $T_{thru(min)}$ are given by

$$T_{drop(max)} = T_{drop}|_{\phi_{rt}=-2\pi m} = \frac{\kappa_1^2\kappa_2^2 a}{(1-t_1t_2a)^2} \ , \tag{2.10}$$

$$T_{drop(min)} = T_{drop}|_{\phi_{rt}=-2\pi(m\pm0.5)} = \frac{\kappa_1^2\kappa_2^2 a}{(1+t_1t_2a)^2} \ , \tag{2.11}$$

$$T_{thru(max)} = T_{thru}|_{\phi_{rt}=-2\pi(m\pm0.5)} = \frac{(t_1+t_2a)^2}{(1+t_1t_2a)^2} \ , \tag{2.12}$$

and

$$T_{thru(min)} = T_{thru}|_{\phi_{rt}=-2\pi m} = \frac{(t_1-t_2a)^2}{(1-t_1t_2a)^2} \tag{2.13}$$

IL$_{drop}$ is defined as the drop-port insertion loss, in dB, at the resonant wavelengths, see Figure 2.6, and is given by

$$IL_{drop} = -10\ log_{10}(T_{drop(max)}) = -10\ log_{10}\left[\frac{\kappa_1^2\kappa_2^2 a}{(1-t_1t_2a)^2}\right] \tag{2.14}$$

OBRR is the ratio, in dB, of the power level at the drop port at resonance to the

minimum power level, see Figure 2.6. The OBRR is given by

$$\text{OBRR} = 10\ log_{10}\left(\frac{T_{drop(max)}}{T_{drop(min)}}\right) = 20\ log_{10}\left(\frac{1+t_1t_2a}{1-t_1t_2a}\right) \tag{2.15}$$

ER is defined as the ratio, in dB, of the maximum power level at the through-port response to the magnitude of the through-port notch at resonance, see Figure 2.6. ER is given by

$$\text{ER} = 10\ log_{10}\left(\frac{T_{thru(max)}}{T_{thru(min)}}\right) = 20\ log_{10}\left[\left(\frac{t_1+t_2a}{t_1-t_2a}\right)\left(\frac{1-t_1t_2a}{1+t_1t_2a}\right)\right] \tag{2.16}$$

Lastly, we will derive an analytical equation for the 3dB-BW of an MRR design. The 3dB-BW is defined as the full-width-at-half maximum power levels. In other words, the 3dB-BW is the difference between the frequencies, f_L and f_H, which occur at the points at which the power levels are equal to half of the peak power level (i.e., when $T_{drop}(f_L) = T_{drop}(f_H) = T_{drop(max)}/2$). This criterion gives

$$\begin{aligned}\frac{\kappa_1^2\kappa_2^2a}{1+(t_1t_2a)^2-2t_1t_2a\ \cos(\phi_L)} &= \frac{\kappa_1^2\kappa_2^2a}{1+(t_1t_2a)^2-2t_1t_2a\ \cos(\phi_H)} \\ &= \frac{\kappa_1^2\kappa_2^2a}{2(1-t_1t_2a)^2}\end{aligned} \tag{2.17}$$

where ϕ_L is the phase at frequency f_L and is given by $\phi_L = \frac{2\pi n_R(f_L)f_L}{c}L_{rt}$ (c is the speed of light), and ϕ_H is the phase at frequency f_H and is given by $\phi_H = -\frac{2\pi n_R(f_H)f_H}{c}L_{rt}$. Here, we assume that if the maximum power level occurs at the resonant frequency, f_r, then f_L occurs at f_r- 3dB-BW$/2$ and f_H occurs at f_r+ 3dB-BW$/2$. After simplifying equation 2.17 and solving for ϕ_L and ϕ_H, we get

$$\phi_H = -\phi_L = \arccos\left[1-\frac{(1-t_1t_2a)^2}{2t_1t_2a}\right] \tag{2.18}$$

We know that $\arccos(1-\frac{x^2}{2}) \simeq x$ for small values of x ($x \ll 1$). Here, $x = \frac{1-t_1t_2a}{\sqrt{t_1t_2a}}$, and x is often close to 0, in our MRR designs, given that $t_1t_2a \approx 1$. Thus, ϕ_L and ϕ_H can be approximated to be

$$\begin{aligned} \phi_L &\simeq \frac{1-t_1t_2a}{\sqrt{t_1t_2a}} \\ &\text{and} \\ \phi_H &\simeq -\frac{1-t_1t_2a}{\sqrt{t_1t_2a}} \ , \end{aligned} \tag{2.19}$$

respectively. The 3dB-BW can be obtained by equating

$$\phi_L - \phi_H = \frac{2\pi n_R(f_H)f_H}{c}L_{rt} \ - \ \frac{2\pi n_R(f_L)f_L}{c}L_{rt} \tag{2.20}$$

Clearly, $\phi_H = -\phi_L$. Equation 2.20 can be then rewritten as

$$2\phi_L = \frac{2\pi L_{rt}n_g}{c}(f_H - f_L) \tag{2.21}$$

where n_g is the group index, which takes into account the effect of dispersion on the effective indicies. After substituting equation 2.19 into equation 2.21 and given that 3dB-BW = $f_H - f_L$, the 3dB-BW is given by

$$\text{3dB-BW} = \frac{c}{\pi n_g L_{rt}}\left(\frac{1-t_1t_2a}{\sqrt{t_1t_2a}}\right) \tag{2.22}$$

Also, from equation 2.22, the bandwidth as the difference in wavelengths, $\Delta\lambda_{3dB}$, can be given by

$$\Delta\lambda_{3dB} \approx \frac{\lambda_r^2}{\pi n_g L_{rt}}\left(\frac{1-t_1t_2a}{\sqrt{t_1t_2a}}\right) \tag{2.23}$$

Equation 2.23 is similar to the equation given in [75] for the bandwidth. The Q-factor measures the ability of an MRR to store energy and is commonly defined as

$$\text{Q-factor} = 2\pi f_r \frac{\text{energy stored in the MRR}}{\text{power dissipated in the MRR}} \tag{2.24}$$

The Q-factor can also be defined as the sharpness of the resonance relative to its center frequency in which case it is given by

$$\text{Q-factor} \equiv \frac{f_r}{\text{3dB-BW}} \tag{2.25}$$

or, in terms of wavelength, is given by

$$\text{Q-factor} \equiv \frac{\lambda_r}{\Delta\lambda_{3dB}} \tag{2.26}$$

Using equations 2.23 and 2.26, the Q-factor can be calculated using the following equation

$$\text{Q-factor} \approx \frac{\pi n_g L_{rt}}{\lambda_r} \left(\frac{\sqrt{t_1 t_2 a}}{1 - t_1 t_2 a} \right) \tag{2.27}$$

2.3 Device Design

A schematic of our proposed MRR with bent couplers is shown in Figure 2.7. Our MRR is composed of two identical bent directional couplers in both of the MRR's coupling regions to form a symmetric add-drop MRR filter. In this section, the procedure to design an MRR with bent directional couplers is described. The MRR has a radius, R, and the bus waveguides have bends in them of radius, $2R$, to connect the couplers to external components. The height of the waveguides is 220 nm and the width of the ring waveguide, W_R, is chosen to be 650 nm. Additionally, the gap width of each of the couplers, g, is chosen to be 200 nm. The MRR is designed with a radius, R, of 2.75 µm so as to obtain an FSR of $\simeq$35 nm (nearly equal to the width of the C-band). For example, taking the group index of a 650 nm wide waveguide to be 4, the FSR of our 2.75 µm MRR would be 34.8 nm at a wavelength of 1550 nm. The width of the bus waveguide, W_B, is then designed according to the phase-match condition for bent waveguides [62]. Here,

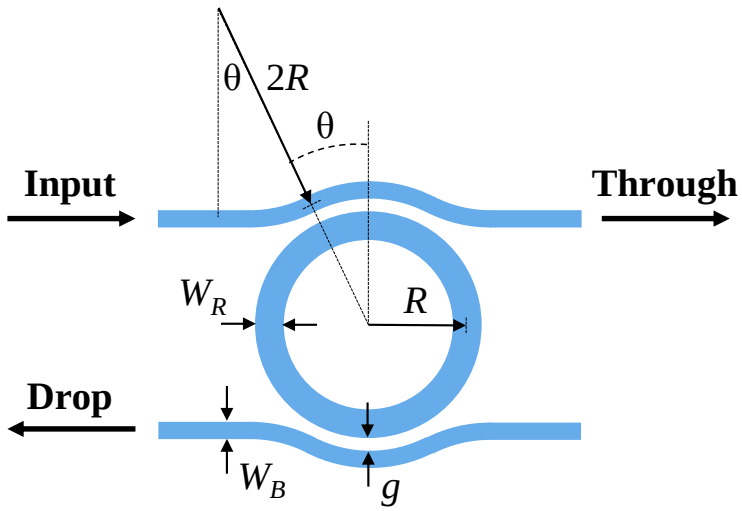

Figure 2.7: A schematic of our MRR with bent couplers.

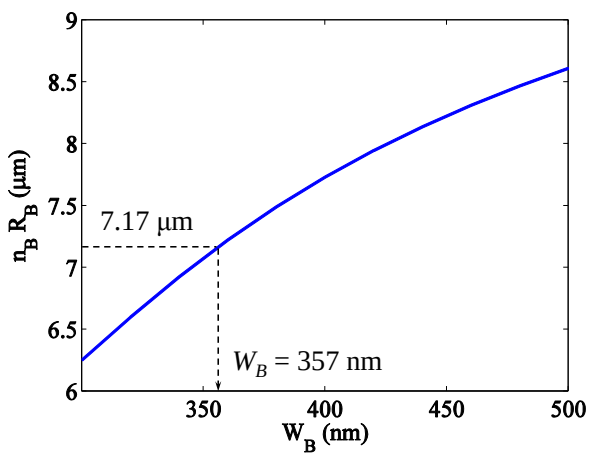

Figure 2.8: A plot of $n_B R_B$ versus W_B of our MRR filter. This plot is used to design the bent couplers, in our filter, for the phase-match condition.

the effective indicies of the ring and bus waveguides, n_R and n_B, are obtained using the eigenmode solver in Lumerical MODE Solutions. Using the plot in Figure 2.8, and given that $W_R = 650$ nm, $g = 200$ nm, and $R = 2.75\,\mu$m, W_B is designed to be 357 nm (at $n_B R_B = n_R R = 7.17\,\mu$m in the plot).

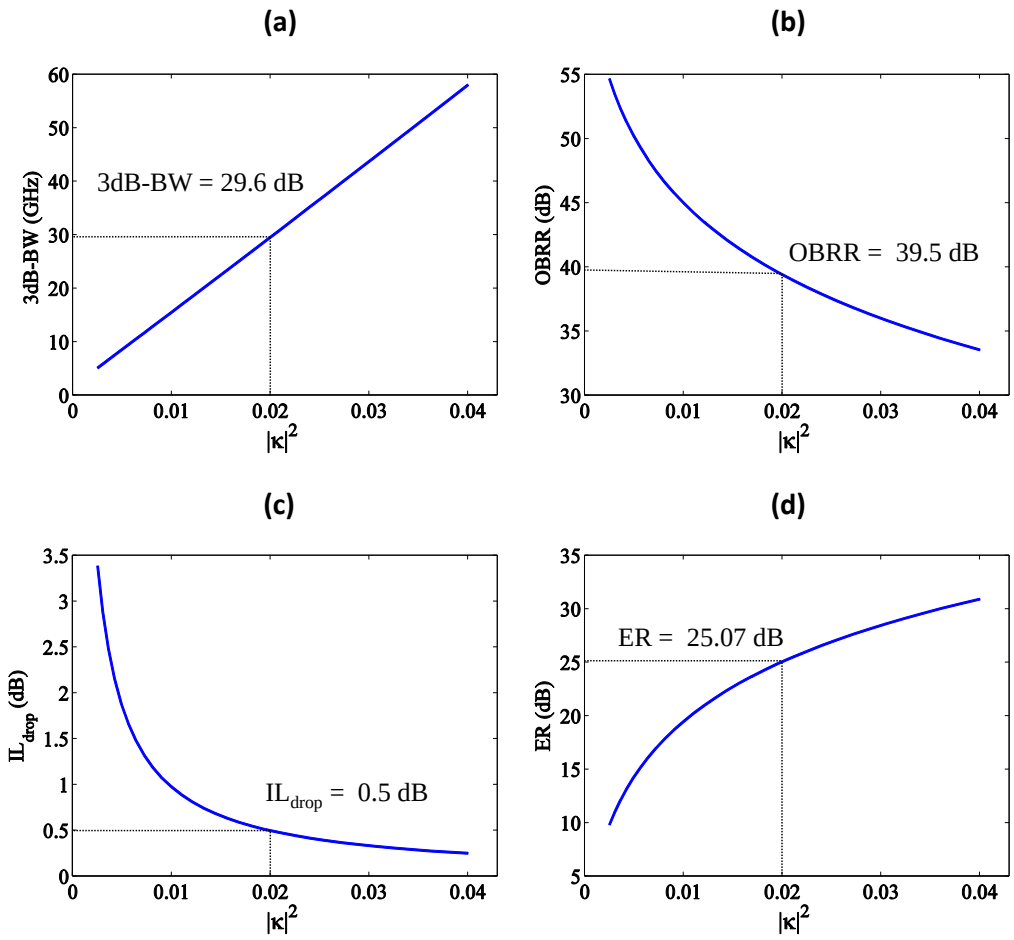

Figure 2.9: Plots of (a) the 3dB-BW, (b) the OBRR, (c) the IL_{drop}, and (d) the ER of a symmetric add-drop MRR filter (R = 2.75 µm) at various $|\kappa|^2$ values.

Lastly, the bend angle, θ, of our MRR couplers is designed. θ is defined as the angle from the vertical to the inflection point of the bent coupler, as illustrated in Figure 2.7. An increase in θ will lead to an increase in the effective coupling length and, consequently, an increase in the power coupling coefficient, $|\kappa|^2$. Thus, in our design procedure the choice of θ depends on our chosen $|\kappa|^2$ value; $|\kappa|^2$ is chosen to obtain the desired 3dB-BW, OBRR, through-port ER, and IL_{drop}. Accordingly, the 3dB-BW, the OBRR, the IL_{drop}, and the ER of a sym-

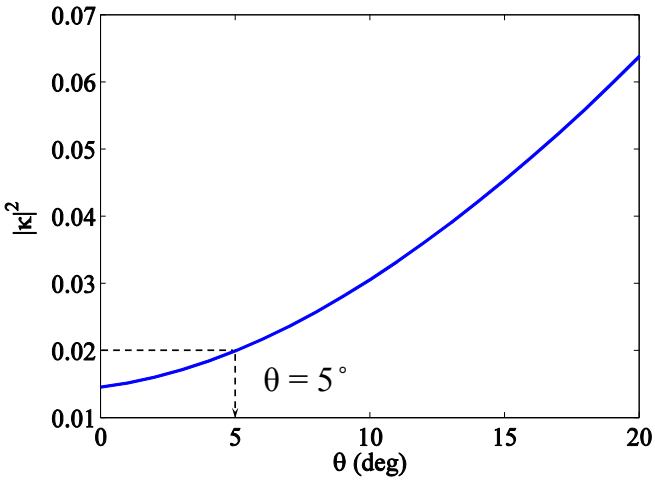

Figure 2.10: A plot of $|\kappa|^2$ at various θ values of the simulated bent couplers.

metric MRR are plotted at various $|\kappa|^2$ values and are shown in Figures 2.9(a), 2.9(b), 2.9(c), and 2.9(d), respectively. In these plots, the IL_{drop}, the OBRR, the ER, and the 3dB-BW are calculated using equations 2.14, 2.15, 2.16, and 2.22, respectively. Here $\kappa_1 = \kappa_2 = \kappa$, and the ring loss is assumed to be 6 dB/cm; this loss is chosen to account for the bending losses in a 2.75 µm radius microring. To obtain a target bandwidth of ∼30 GHz, a $|\kappa|^2$ value of 0.02 is chosen for our MRR design, see Figure 2.9(a). In addition, at our chosen $|\kappa|^2$ value of 0.02, the OBRR $\simeq$ 40 dB (see Figure 2.9(b)), the IL_{drop} = 0.5 dB (see Figure 2.9(c)), and the ER $\simeq$ 25 dB (see Figure 2.9(d)). Accordingly, our chosen MRR filter design should follow most of the target specifications presented in [76]. Our bent directional coupler is then simulated, in 3D, using Lumerical FDTD Solutions. In these simulations, θ is swept (from 0° to 20°) and the resulting $|\kappa|^2$ values are collected for each of the θ values. A plot of $|\kappa|^2$ at various θ values for our simulated bent couplers (using FDTD Solutions) is shown in Figure 2.10. The simulations indicate that a θ of 5° be chosen for our design as it will result in the desired coupling ($|\kappa|^2 = 0.02$) as seen in Figure 2.10. Using equations 2.8 and 2.9, the responses at the drop and through ports of our designed MRR filter are shown in Figure 2.11.

From these responses, our MRR filter achieved an FSR of ∼35 nm, which will span most of the C-band.

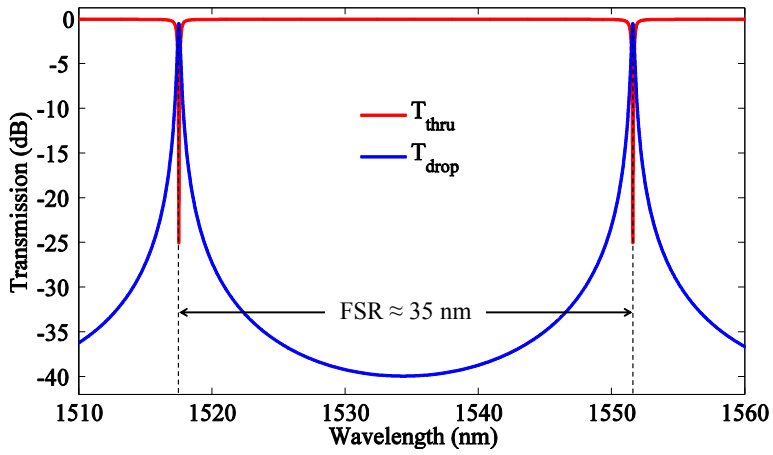

Figure 2.11: Theoretical responses of our MRR filter, at the drop port and at the through port, when $|\kappa|^2 = 0.02$.

2.4 Layout and Fabrication

In order to account for fabrication variations, MRRs with various values of θ and W_B were fabricated. For all variations, g and W_R are kept constant at 200 nm and 650 nm, respectively. Table 2.1 summarizes the design variations for our MRR filter. Our filter was fabricated using 248 nm deep-UV photolithography at the IME A*STAR foundry. The waveguides are 220 nm in height and have a top oxide cladding. Metal TiN heaters are also used on top of the waveguides for thermal tuning; the metal heaters are 2 µm wide. Additionally, deep trenches in the oxide and silicon undercuts, similar to the ones described in [77], are used. The deep trenches are 10 µm wide and are placed ∼2.3 µm away from the MRRs' waveguides. The air trenches surround each of our MRRs for thermal isolation. Also, some of the underlying silicon beneath the MRRs' waveguides and between the trenches is removed to form silicon undercuts. The air trenches and the undercuts are intended to improve the tuning efficiency. Also, a total of three grating

couplers (GCs) are used for each of our MRRs; one GC is connected to the input port of the MRR to couple light into the filter and the other two GCs are each connected to the drop port and the through port to couple light out of the filter. The GCs are optimized to couple TE-polarized light and to operate around a laser wavelength of 1550 nm.

Table 2.1: MRR with bent couplers filter design parameter variations.

Design Parameter	Variations
R	2.75 µm
W_B	340 nm, 350 nm, 357 nm, 370 nm
W_R	650 nm
g	200 nm
θ	5°, 10°, 20°

2.5 Measurement Results and Discussion

The spectral responses of our fabricated MRR filters are measured and their $|\kappa|^2$ values are extracted using a method similar to the one presented in [78]. The extracted $|\kappa|^2$ for the MRR with W_B = 370 nm and θ = 5° was 0.017 and was the closest to the desired value of 0.02. The MRR with the next closest $|\kappa|^2$ of 0.012 was the one with W_B = 357 nm and θ = 5°. Therefore, the MRR with W_B = 370 nm has results that are closest to the theoretical results shown in Figure 2.11. Hence, the results for the MRR with W_B = 370 nm, θ = 5°, W_R = 650 nm, g = 200 nm, and R = 2.75 µm are presented.

Figures 2.12(a) and 2.12(b) show the spectral responses of our MRR filter. The MRR has an FSR of 33.4 nm, which is close to the designed value of 35 nm. Figure 2.12(b) shows a zoomed-in plot of the normalized (with respect to the

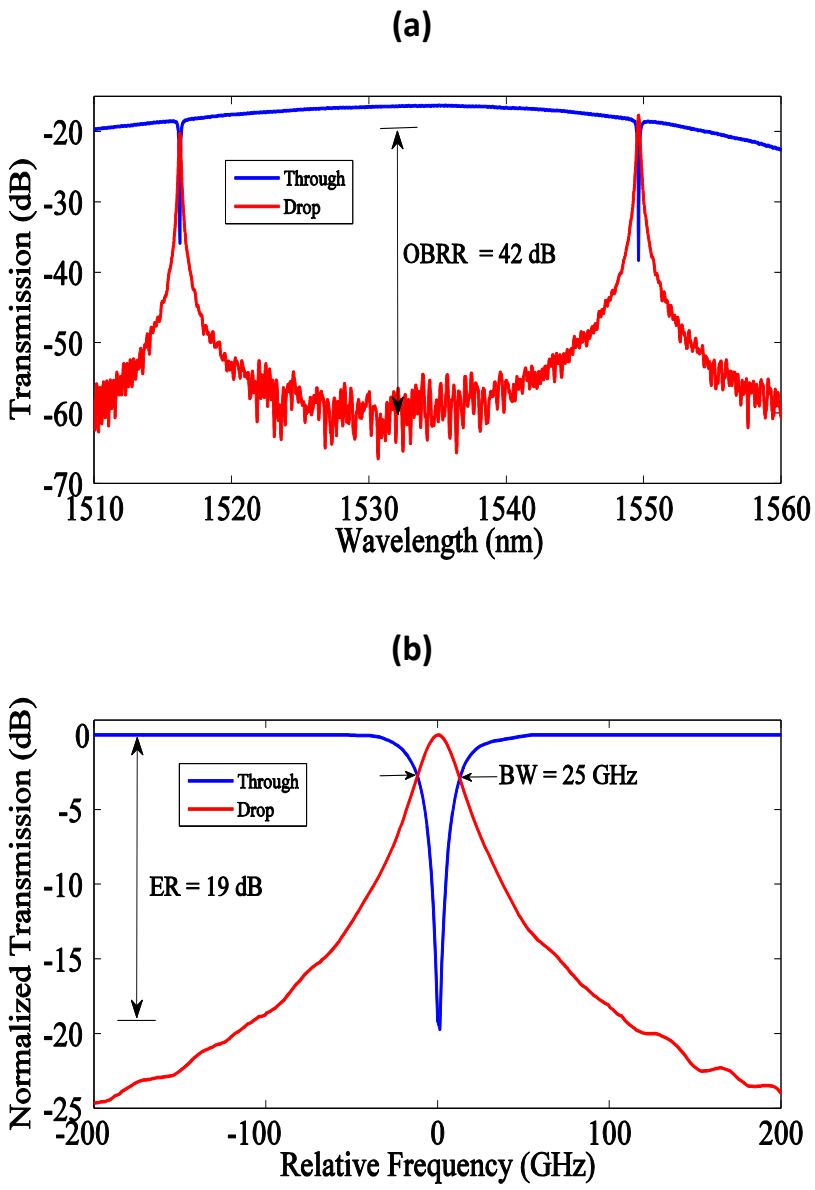

Figure 2.12: (a) Measured spectral responses of the through and drop ports over the wavelength range 1510 nm to 1560 nm. (b) Normalized spectral responses, in GHz, at the through and drop ports for the resonance at 1549.6 nm.

GCs responses) through and drop port spectral responses around the resonance at 1549.6 nm. The 3dB-BW of the MRR is 25 GHz, which is also close to the design value. This MRR also has an ER of 19 dB, an OBRR of 42 dB, and an IL_{drop} of less than 1 dB. These measured results are summarized in Table 2.2; also, the theoretical results calculated in section 2.3 are included in the table for comparison purposes. From Table 2.2, the measured results (3dB-BW, OBRR, IL_{drop}, and ER) are all smaller than the theoretical results. This could be because $|\kappa|^2$ of the fabricated device is less than that of the simulated device. Also, the measured FSR of our device is smaller than the expected (theoretical) value. The measured FSR may be smaller because the theoretical FSR value is calculated using the group index of a straight waveguide despite the ring waveguide of our MRR being bent. In a bent waveguide with $R = 2.75\,\mu m$ the group index is larger than that of a straight waveguide, see Figure 2.4(b). As a result, the group index of the fabricated device (of a 2.75 µm bent waveguide) will be larger than the group index used (of a straight waveguide) to theoretically calculate the FSR of our MRR; hence, the measured FSR is smaller than the theoretical one. The drop-port responses of our MRR are measured at various total tuning powers, and the responses are shown in Figure 2.13(a). In each of these measurements, power is applied to the TiN heater

Table 2.2: Summary of the theoretical and measured results of our MRR filter with bent couplers.

Parameter	Theoretical	Measured
FSR (nm)	35	33.4
3dB-BW (GHz)	30	25
OBRR (dB)	40	42
IL_{drop} (dB)	0.5	< 1
ER (dB)	25	19
$\|\kappa\|^2$	0.02	0.017

to shift the drop-port peak wavelength, and the wavelength shift is plotted versus the tuning power in Figure 2.13(b). Our MRR filter with bent couplers has a tuning efficiency, η, of $\sim$12 mW/FSR; the improved tuning efficiency is attributed to the deep trenches and the silicon undercuts.

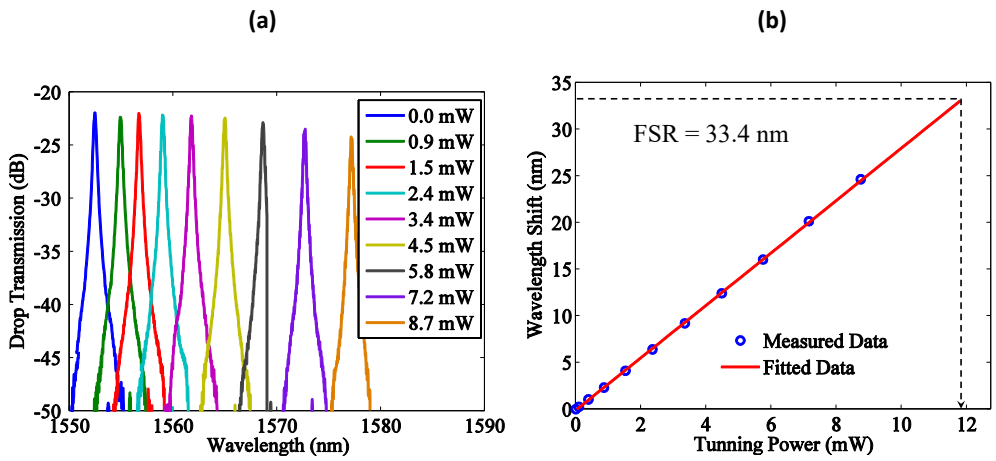

Figure 2.13: (a) Drop-port responses at various total tuning powers. (b) Plot of the total tuning power versus wavelength shift.

The extracted $|\kappa|^2$s of the MRRs with W_B = 370 nm and various values of θ are compared to the $|\kappa|^2$ values obtained from FDTD simulations. A point coupler is also simulated and is designated as the $\theta = 0°$ coupler. These results are shown in Figure 2.14. The $\theta = 0°$ coupler has the lowest $|\kappa|^2$ value, and, therefore, the point-coupled MRR would have the smallest bandwidth. $|\kappa|^2$ increases as θ increases due to the longer effective coupling lengths. This, in turn, leads to an increase in the MRR's 3dB-BW and the ER. This is demonstrated in Figure 2.15, which shows the normalized measured spectral responses of the through and drop ports for three MRRs with different θ values. The through and drop responses were normalized to the grating couplers' responses. The drop port responses were further normalized to their peak values. The bandwidths of the MRRs increase from 25 GHz at $\theta = 5°$ to 37 GHz at $\theta = 10°$ to 71 GHz at $\theta = 20°$. This demonstrates that, by using bent couplers, MRRs with ultra-wide bandwidths and large FSRs can be realized.

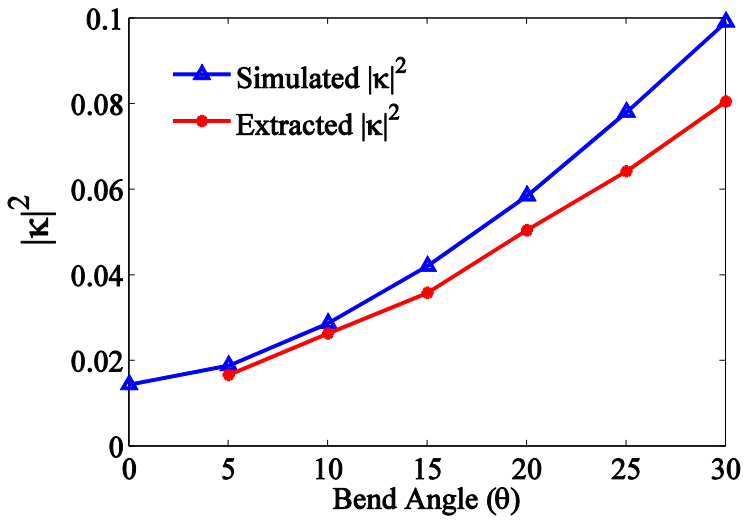

Figure 2.14: (a) The power coupling coefficient, $|\kappa|^2$, from measurement data and FDTD simulations, versus θ.

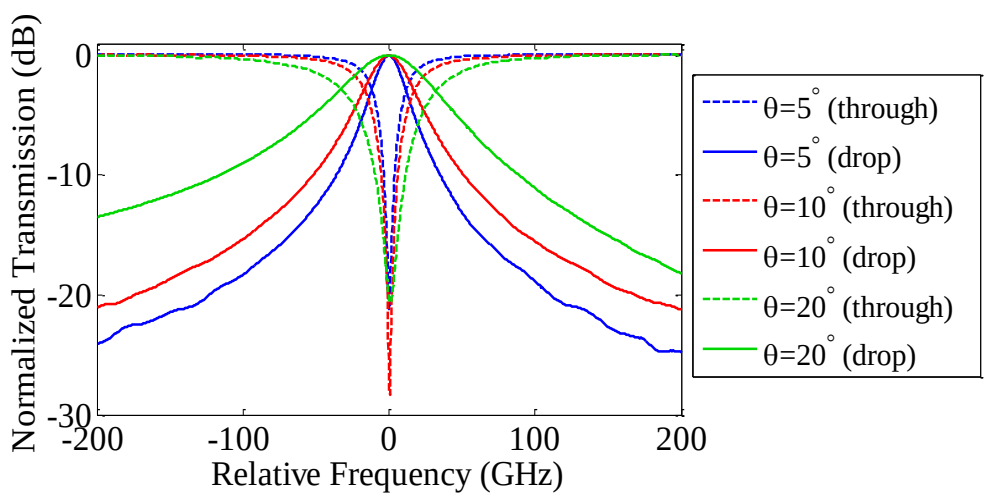

Figure 2.15: Measured spectral responses, in GHz, at the through (dashed lines) and drop ports (solid lines) for θ = 5° (blue), θ = 10° (red), and θ = 20° (green).

Lastly, our MRR performance is compared to other state-of-the-art single-ring MRR filters; the compared results are shown in Table 2.3. The footprints provided in the table are estimated based on the R and L_c values of the MRRs as $\pi R^2 + 2RL_c$. The MRR demonstrated in [79] was thermally tuned using TiN heaters and had air trenches around the MRR and the MRR demonstrated in [80] was also tuned using TiN heaters and had both air trenches and silicon undercuts. However, the MRR demonstrated in [81] was electrically tuned using PiN doping in the waveguides and achieved an OBRR of 28 dB, an IL_{drop} of 1.3 dB, and an ER greater than 15 dB. Clearly, the OBRR and the ER of the MRR in [81] are less than those of our MRR and its IL_{drop} is greater than that of our MRR. From Table 2.3, our device has the smallest footprint because it has the smallest R and it is a ring not a racetrack (i.e., L_c = 0). In addition, our MRR has the smallest η as compared to the other devices. Finally, our device has one of the widest FSRs because it has the shortest roundtrip length.

Table 2.3: Comparison of our MRR filter with other single-ring MRR filters.

Parameter	Our device	P. Dong, *et al.* [79]	P. Dong, *et al.* [80]	Z. Su, *et al.* [81]
R (μm)	2.75	4	4	3
L_c (μm)	0	2	11	0
FSR (nm)	33.4	19	11.5	34
3dB-BW (GHz)	25	25	25	59.5
η (mW/FSR)	12	21	2.4	31
Footprint (μm^2)	24	66	138	28

2.6 Summary

A compact MRR based filter with a radius of 2.75 µm, that uses bent directional couplers to increase the power coupling coefficient, has been studied. Bent directional couplers allow for gaps that are large enough to be fabricated using optical lithography, thereby making compact MRR filters with large FSRs amenable to mass-production in CMOS-compatible processes. In this chapter, a brief overview of bent directional couplers and the MRRs that use them has been presented, as well as the design procedure used to design MRRs with bent directional couplers. Measurements show that our filter exhibits a wide FSR of 33.4 nm, while achieving a 3dB-bandwidth of 25 GHz, a through-port extinction ratio of 19 dB, and a low drop-port insertion loss. Finally, it is shown that by using bent couplers, θ can be used to control a small radius MRR's bandwidth while maintaining a large FSR.

Chapter 3

FSR-Free Silicon-on-Insulator Microring Resonator Based Filter with Bent Contra-Directional Couplers

High-speed optical interconnects drive the need for compact MRR filters with wide FSRs and with wide bandwidths [17, 41]. MRR based filters that integrate straight CDCs (contra-directional couplers) in the coupling regions of racetrack resonators have been previously demonstrated [55, 82, 83]. By proper design, integrating CDCs in an MRR's coupling regions can suppress the undesired longitudinal modes of the MRR and eliminate the FSR. In other words, all of the MRRs longitudinal modes, except for the one that aligns with the CDCs main lobes are suppressed. As a result, FSR-free responses can be obtained. In these designs, the CDCs increase the footprints of the filters as compared to standard microring and racetrack resonators. However, by partially wrapping the CDCs around the MRR, we demonstrate that MRRs with CDCs can be smaller than those previously demonstrated. Additionally, MRRs with bent CDCs allow for filter designs that can have large side-mode suppressions; this can be difficult to

achieve using MRRs with straight CDCs. Hence, by utilizing bent CDCs in an MRR design, a filter is realized that has a more compact footprint, has a relatively large side-mode suppression, and has a wide bandwidth while having ”FSR-free” responses at both the drop and through ports. Here, by ”FSR-free” we mean that our filter significantly suppresses the MRR side modes; achieving an amplitude response that appears as though it has no FSR. In this chapter, we will first give a brief introduction to CDCs: both straight CDCs and bent CDCs. Then, we will describe the design procedure and present the experimental results of our MRR based filter with bent CDCs.

3.1 Contra-directional Couplers

3.1.1 Overview

CDCs have been proposed as add-drop filters due to their wavelength selective natures [84]. CDCs are composed of two asymmetric waveguides with corrugations on each of the waveguides' side-walls as shown in the schematic in Figure 3.1. Here, the corrugations are achieved by applying periodic perturbations to the widths of the waveguides; the perturbations have corrugations depths of ΔW_B and ΔW_R for waveguides B and R, respectively. The gratings on the inner side-walls cause contra-directional coupling between the forward propagating mode in one waveguide (waveguide B) and the backward propagating mode in the other waveguide (waveguide R). In order to suppress the CDCs' Bragg reflections, anti-reflection gratings are used at the external side-walls of the waveguides, in which the gratings are out-of-phase with the gratings used at the inner side-walls [85].

Contra-directional coupling occurs when the forward propagating mode in waveguide B is in-phase with the backward propagating mode in waveguide R (this causes constructive interference between these modes) [86]. In other words, contra-directional coupling occur when the difference between the phases of the forward local normal mode and of the backward local normal mode, after each

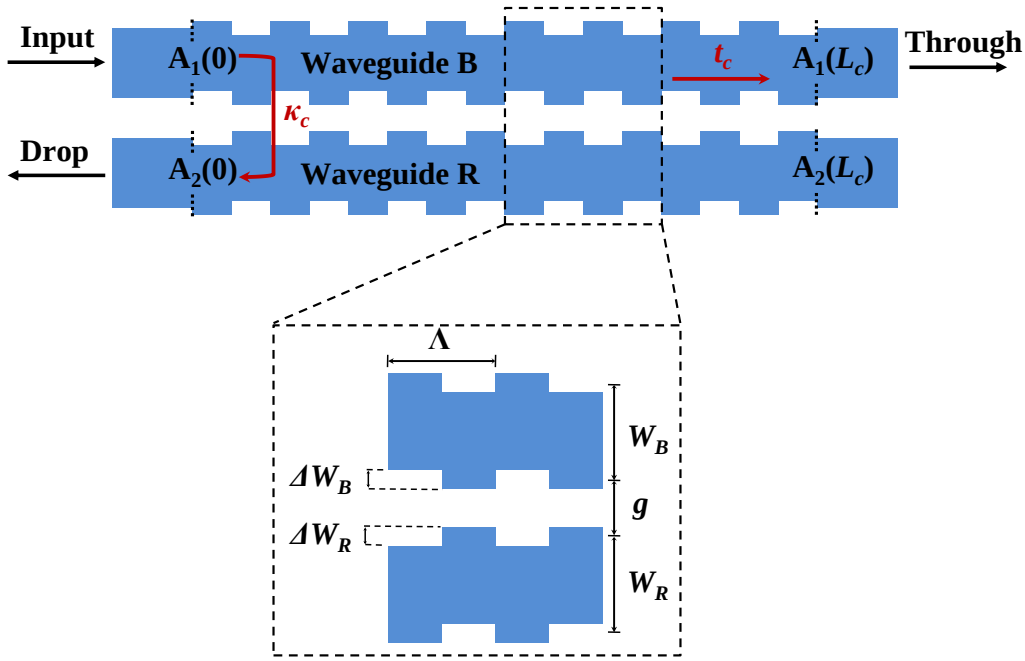

Figure 3.1: A schematic of a straight CDC that has a coupling length of L_c. The inset shows a zoomed-in section of the CDC with design parameters illustrated on it.

perturbation, is 2π; this gives

$$\beta_B \Lambda + \beta_R \Lambda = 2\pi \tag{3.1}$$

where Λ is the perturbation period, β_B and β_R are the propagation constants in waveguides B and R, respectively, and

$$\beta_B = \frac{2\pi n_B(\lambda_o)}{\lambda_o} \tag{3.2}$$

and

$$\beta_R = \frac{2\pi n_R(\lambda_o)}{\lambda_o} \tag{3.3}$$

where λ_o is the wavelength in free space, and n_B and n_R are the effective indicies of waveguides B and R, respectively. Because β_B and β_R change with wavelength, equation 3.1 is only satisfied at a wavelength λ_D. λ_D is the wavelength at which contra-directional coupling occurs. Accordingly, the phase-match condition for a CDC becomes

$$\Lambda = \frac{\lambda_D}{n_B(\lambda_D) + n_R(\lambda_D)} \tag{3.4}$$

Clearly, λ_D depends on Λ, n_B, and n_R; the effective indicies, n_B, and n_R, depend on the widths of waveguides B and R, W_B and W_R, respectively. Thus, one of the design procedures for CDCs is to determine Λ for a target λ_D and for the chosen waveguide widths. This is done by solving the phase-match condition given in equation 3.4.

Besides contra-directional coupling, there are Bragg reflections in each of the waveguides, B and R, [50]. The reflections in waveguide B occur at wavelength, λ_B, which is determined by the phase-match condition, $2\beta_B\Lambda = 2\pi$. Also, the reflections in waveguide R occur at λ_R, which is determined by the phase-match condition, $2\beta_R\Lambda = 2\pi$. Figure 3.2 summarizes the three phase-match conditions for the wavelengths: λ_D, λ_B, and λ_R. Here, n_B and n_R are obtained by simulating each of the waveguides B and R using Lumerical MODE Solutions. In this simulation, each of the waveguides is simulated individually for simplicity. The parameters of the waveguides of the CDC are: W_B = 450 nm, W_R = 550 nm, and Λ = 318 nm.

The responses of a CDC at the drop port and at the through port are determined using coupled-mode theory [87]. The coupled equations (shown below) relate the forward propagating mode in waveguide B (A_1) to the backward propagating mode in waveguide R (A_2) and vice versa. In these equations co-directional coupling is assumed to be negligible. In the case of contra-directional coupling, the coupled equations are given by

$$\frac{d}{dz}A_1 = -j\kappa_o A_2(z)e^{j\Delta\beta z} \tag{3.5}$$

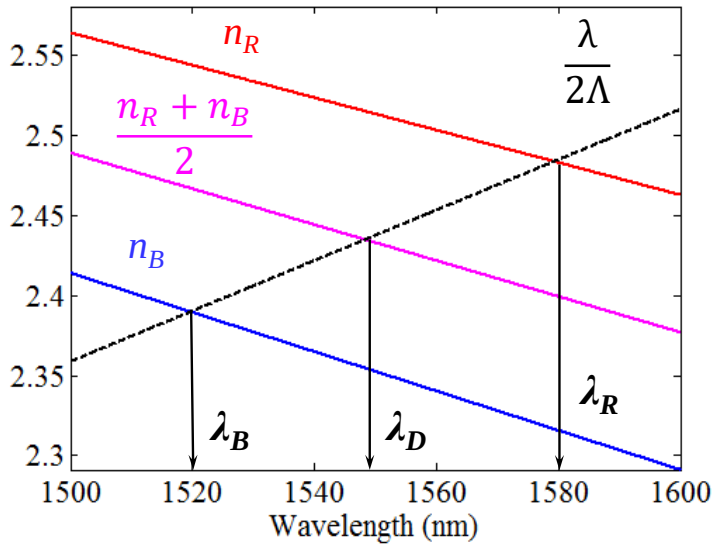

Figure 3.2: Plot illustrating the phase-match conditions of a straight CDC for wavelengths λ_D, λ_B, and λ_R.

and

$$\frac{d}{dz}A_2 = j\kappa_o A_1(z)e^{-j\Delta\beta z} \tag{3.6}$$

where $\Delta\beta$ is the phase mismatch between the modes, and κ_o is the magnitude of the distributed coupling coefficient. Also, in these equation the forward propagating mode is assumed to be propagating in the +z direction. Solving equations 3.5 and 3.6 we get

$$A_1(z) = e^{j\frac{\Delta\beta}{2}z}\frac{s\ \cosh(s(L_c - z)) + j\frac{\Delta\beta}{2}\sinh(s(L_c - z))}{s\ \cosh(sL_c) + j\frac{\Delta\beta}{2}\sinh(sL_c)}A_1(0) \tag{3.7}$$

and

$$A_2(z) = e^{-j\frac{\Delta\beta}{2}z}\frac{-j\kappa_o \sinh(s(L_c - z))}{s\ \cosh(sL_c) + j\frac{\Delta\beta}{2}\sinh(sL_c)}A_1(0) \tag{3.8}$$

where L_c is the coupling length of the CDC. As a result, the electric field transfer functions of a CDC at the drop port, κ_c, and at through port, t_c, are given by

$$\kappa_c = \frac{A_2(0)}{A_1(0)} = \frac{-j\kappa_o \sinh(sL_c)}{s\ \cosh(sL_c) + j\frac{\Delta\beta}{2}\sinh(sL_c)} \tag{3.9}$$

and

$$t_c = \frac{A_1(L_c)}{A_1(0)} = \frac{s\ e^{j\frac{\Delta\beta}{2}L_c}}{s\ \cosh(sL_c) + j\frac{\Delta\beta}{2}\sinh(sL_c)}\ , \tag{3.10}$$

respectively, where, $s^2 = \kappa_o^2 - (\frac{\Delta\beta}{2})^2$ and $\Delta\beta = \frac{2\pi n_B}{\lambda} + \frac{2\pi n_R}{\lambda} - \frac{2\pi}{\Lambda}$.
κ_o is the coupling coefficient per unit length and is a representation of the coupling strength of a CDC. κ_o increases as the coupler's gap between waveguide B and waveguide R decreases, and as ΔW_B or ΔW_R increases. The magnitude responses, in dB, of equations 3.9 and 3.10 are shown in Figure 3.3. The CDC, for which we have plotted the responses, has the following parameters: W_B = 450 nm, W_R = 550 nm, Λ = 318 nm, L_c = 200 µm, and $\kappa_o \simeq$ 10000 m$^-$1.

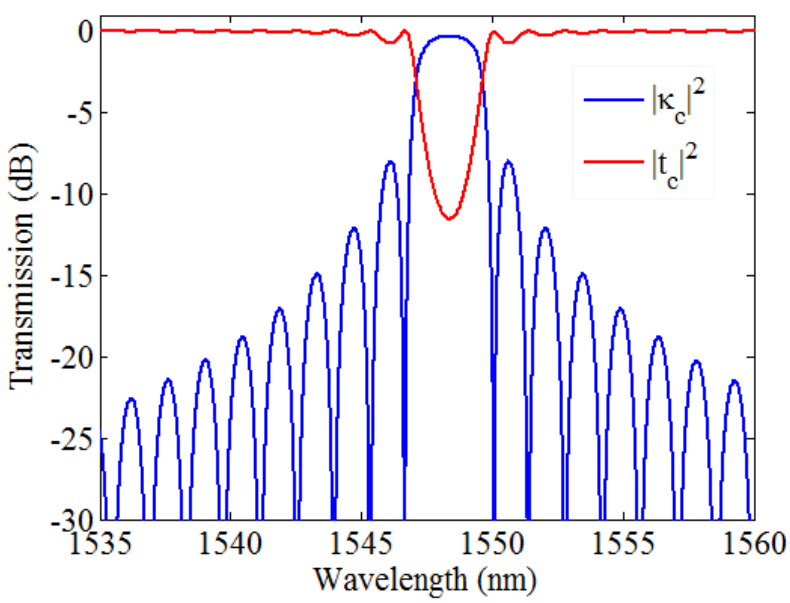

Figure 3.3: Plots of the magnitude-squared responses of a CDC at the drop port ($|\kappa_c|^2$) and at the through port ($|t_c|^2$).

3.1.2 Bent CDCs

In bent CDCs one of the waveguides (waveguide B) is partially wrapped around the other waveguide (waveguide R) as shown in Figure 3.4. This is a similar design to a bent directional coupler (discussed in chapter 2), but with periodic perturbations being used on the side-walls of the waveguides. The design parameters, illustrated in Figure 3.4, for the CDCs include: the widths of the waveguides, W_B and W_R, the corrugation depths, ΔW_B and ΔW_R, the couplers' gap widths, g, and Λ. In bent CDCs, Λ is measured at the center of the coupler's gap as shown in Figure 3.4. Clearly, the design parameters of bent CDCs are the same as those of straight CDCs. Also, equations 3.9 and 3.10, for the drop port and the through port responses, are the same as in bent CDCs.

However, the phase-match conditions for straight CDCs are modified for bent CDCs to account for the changes in the perturbation period as we move away and/or towards the side-walls of waveguides B and R. Specifically, in bent CDCs waveguides B and R have different bend radii, R_B and R, respectively. This causes the perturbation period measured at the center of waveguide B (Λ_B) to be different from the perturbation period measured at the center of waveguide R (Λ_R); which is not the case in straight CDCs. Here, we assume that the phase-match conditions approximately depend on Λ_B and Λ_R, which are measured at the centers of the waveguides. Takings these facts into account, we will modify the phase-match condition for contra-directional coupling. Accordingly, the condition for constructive interference between the forward and backward propagating modes in bent CDCs becomes

$$\beta_B \theta_\Lambda R_B + \beta_R \theta_\Lambda R \cong 2\pi \tag{3.11}$$

where, θ_Λ, illustrated in Figure 3.4, is the bend angle of each perturbation and is given by

$$\theta_\Lambda = \frac{\Lambda}{R + \frac{W_R}{2} + \frac{g}{2}} \tag{3.12}$$

Also, R_B is given by $R_B = R + \frac{W_R}{2} + g + \frac{W_B}{2}$. Substituting equations 3.2 and 3.3

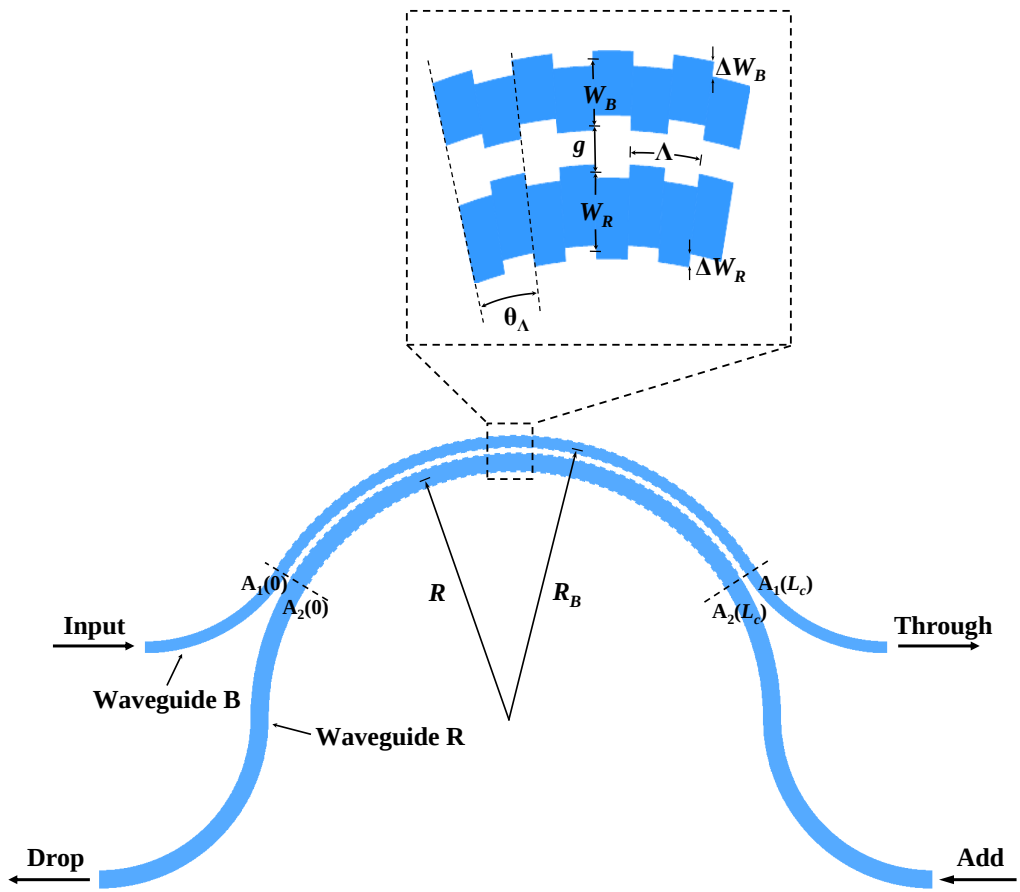

Figure 3.4: A schematic of a bent CDC that has a coupling length of L_c. The inset shows a zoomed-in section of the CDC on which the design parameters and the bend angle, θ_Λ, are illustrated.

into equation 3.11 we get

$$\frac{2\pi n_B(\lambda_D)}{\lambda_D}\theta_\Lambda R_B + \frac{2\pi n_R(\lambda_D)}{\lambda_D}\theta_\Lambda R \cong 2\pi \tag{3.13}$$

Rearranging equation 3.13 we get

$$\lambda_D \cong \theta_\Lambda(n_B R_B + n_R R) \tag{3.14}$$

We can now solve for Λ and our phase-match condition, for contra-directional coupling, for bent CDCs becomes

$$\Lambda = \frac{\lambda_D(R + \frac{W_r}{2} + \frac{g}{2})}{n_b(R + \frac{W_b}{2} + g + \frac{W_r}{2}) + n_r R} \tag{3.15}$$

Additionally, the phase-match conditions for the wavelengths of the Bragg reflections, λ_B and λ_R, will be different in bent CDCs as compared to straight CDCs. Here, we assume that λ_B and λ_R are approximately determined by Λ_B and Λ_R, respectively. Accordingly, in bent CDCs, λ_B is given by $\lambda_B \approx 2n_B R_B \theta_\Lambda$ and λ_R is given by $\lambda_R \approx 2n_R R \theta_\Lambda$. We will then study an MRR filter that uses bent CDCs in its coupling regions.

3.2 Motivation

Until now there has only been one type of MRR with CDCs integrated in the coupling regions and that is MRRs with straight CDCs. Here we are introducing another type of MRR with CDCs: the MRR with bent CDCs. Typically, in an MRR with straight CDCs, two identical straight CDCs are used as the couplers of a racetrack resonator with the CDCs having coupling lengths, L_c, and with the bend radii of the racetrack being R_{st}, see Figure 3.5(a). In our MRR with bent CDCs, two identical bent CDCs are used as the couplers to a microring with the CDCs having coupling lengths, L_c, and with the radius of the MRR being, R, see Figure 3.5(b). In this chapter, we show that MRRs with bent CDCs can achieve larger side-mode suppressions than similar MRRs with straight CDCs.

In order for an MRR with CDCs to attain maximum side-mode suppressions, the MRR's side modes should coincide with the nulls of the CDCs, as shown in Figure 3.6, and therefore, the spacings between the first CDCs' nulls, $\Delta\lambda_{null}$, should be equal to twice the MRR's FSR. The spacing $\Delta\lambda_{null}$ of a CDC and the

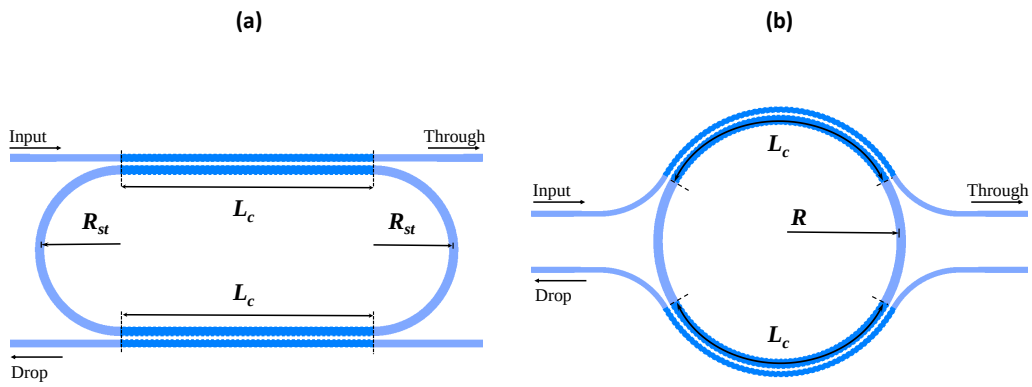

Figure 3.5: (a) A schematic of an MRR with straight CDCs and (b) a schematic of an MRR with bent CDCs. The dark waveguide sections in both of the schematics are the CDCs.

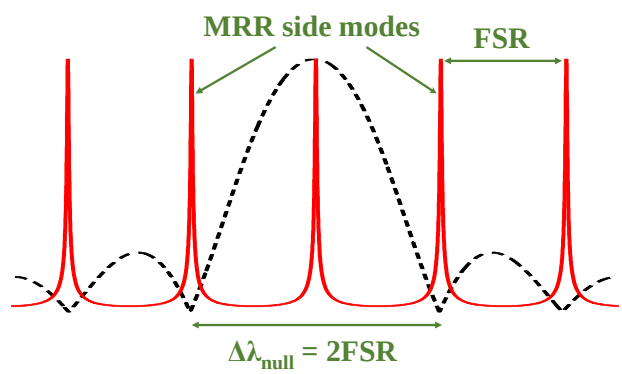

Figure 3.6: A CDC's spectral response (dashed trace) and an MRR's response (solid trace) when $\Delta\lambda_{null}$ = 2FSR.

FSR of an MRR are given by

$$\Delta\lambda_{null} = \frac{2\lambda^2}{\pi(n_{g_R} + n_{g_B})}\sqrt{\kappa_o^2 + (\frac{\pi}{L_c})^2} \tag{3.16}$$

and

$$\text{FSR} = \frac{\lambda^2}{L_{rt} n_{g_R}} \ , \tag{3.17}$$

respectively, and where κ_o is the distributed coupling coefficient for a CDC (L_c

and κ_o are the same for each of the two CDCs), and n_{g_R} and n_{g_B} are the ring and bus waveguides' group indicies, respectively. Also, L_{rt} is the roundtrip length of an MRR; in an MRR with straight CDCs, $L_{rt} = 2\pi R_{st} + 2Lc$, and in an MRR with bent CDCs, $L_{rt} = 2\pi R$. Consequently, for an MRR with straight CDCs to achieve $\Delta\lambda_{null}$ =2FSR, R_{st} of the racetrack should satisfy the following relation,

$$R_{st} = \frac{\frac{n_{g_R}+n_{g_B}}{n_{g_R}}}{2\sqrt{\kappa_o^2 + (\frac{\pi}{L_c})^2}} - \frac{L_c}{\pi} \tag{3.18}$$

In addition, for an MRR with bent CDCs to achieve $\Delta\lambda_{null}$ =2FSR, L_c of each of the CDCs should satisfy the relation,

$$L_c = \frac{2\pi}{\sqrt{\left(\frac{n_{g_R}+n_{g_B}}{n_{g_R}R}\right)^2 - (2\kappa_o)^2}} \tag{3.19}$$

Using equation 3.18, the R_{st} required to satisfy $\Delta\lambda_{null}$ =2FSR is calculated at various values of L_c. Also, using equation 3.19, the L_c required to satisfy $\Delta\lambda_{null}$ =2FSR, is calculated at various values of R. Using the R_{st} and L_c values obtained from equations 3.18 and 3.19, we then calculate $\gamma = (2L_c/L_{rt}) * 100$, where γ is the percentage of coverage of the roundtrip length of the MRR by the CDCs. γ is plotted versus various L_{rt} values in Figure 3.7 for MRRs with straight CDCs and for MRRs with bent CDCs each for κ_o = 2000 m^{-1} and κ_o = 8000 m^{-1}. Here, in these plots, we chose the widths of the ring waveguides of the bent CDCs and the straight CDCs to be the same and to be 550 nm, as well as we chose the widths of the bus waveguides of the bent CDCs and the straight CDCs to be the same and to be 450 nm. Clearly, in the MRRs with bent CDCs, we can fit both of the CDCs on the microrings' circumference ($\gamma < 100\%$) for all of our plotted L_{rt} values. Accordingly, an MRR with bent CDCs can be designed so that the MRR's longitudinal modes are aligned with the CDCs' nulls, and hence maximum side-mode suppressions can be achieved. On the other hand, in the MRR with straight CDCs, $\gamma > 100\%$ for all of our plotted L_{rt} values. In other words, there is no physical

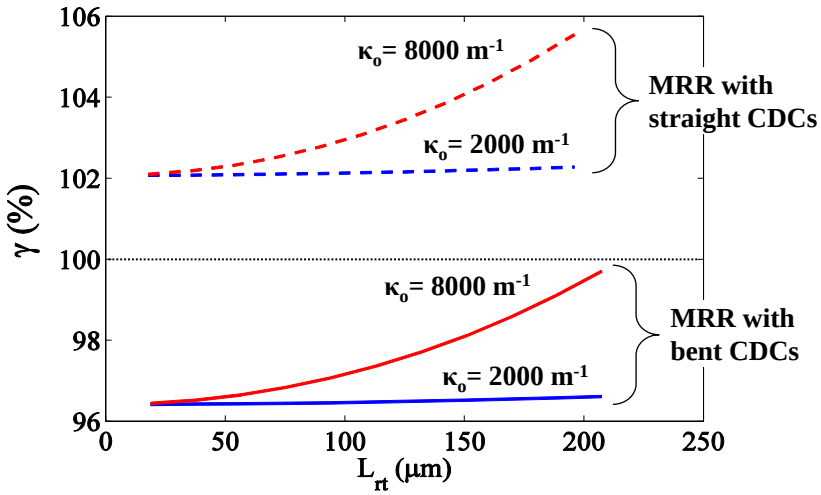

Figure 3.7: Plots of the required MRR's coverage with the CDCs (γ) to achieve maximum suppression versus L_{rt} for MRRs with straight CDCs and MRRs with bent CDCs.

MRR design that exists that can satisfy $\Delta\lambda_{null}$ =2FSR and achieves maximum suppression. This is because the group indicies of the waveguides of a straight CDC are typically smaller than the group indicies of the waveguides of a bent CDC with the same waveguide widths; this causes $\Delta\lambda_{null}$ of a straight CDC to be larger than $\Delta\lambda_{null}$ of a bent CDC. As a result, the L_c value required for an MRR with bent CDCs to achieve $\Delta\lambda_{null}$ = 2FSR will be less than that of an MRR with straight CDCs with the same κ_o and L_{rt} values.

Furthermore, an MRR with bent CDCs and with a large γ value will typically have a larger side-mode suppressions than an MRR with straight CDCs with the same γ value. This is because, in an MRR with straight CDCs, as the coupling lengths of the CDCs are increased, to decrease $\Delta\lambda_{null}$, the roundtrip length of the racetrack resonator decreases and the FSR of the MRR increases. Hence, this can cause the FSR to increase at a greater rate than the decrease in $\Delta\lambda_{null}$, which leads to decreased suppression. However, in an MRR with bent CDCs increasing the coupling lengths of the CDCs will not effect the roundtrip length of the microring. As a result, $\Delta\lambda_{null}$ can be decreased without changing the FSR of the MRR which

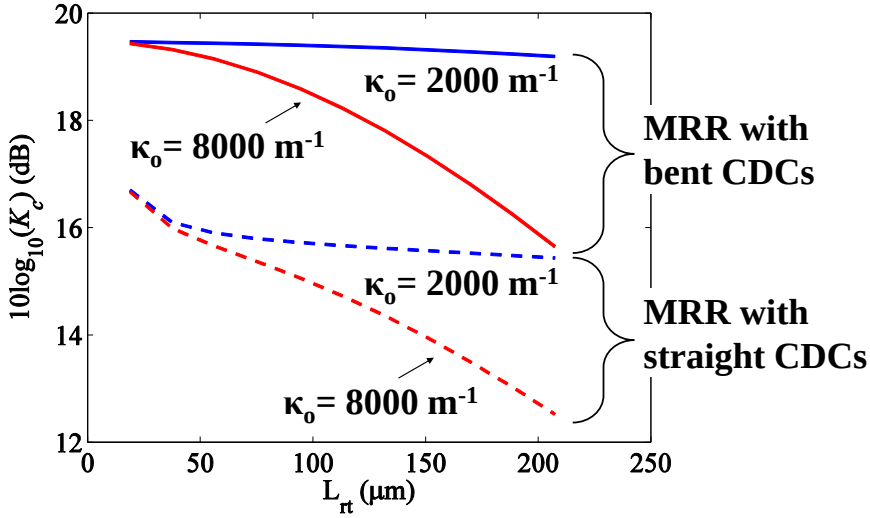

Figure 3.8: Plots of K_c, in dB, versus L_{rt} for MRRs with straight CDC and MRRs with bent CDCs at $\gamma = 87\%$.

leads to an increase in suppression. For illustration purposes, a measure of side-mode suppression, K_c, is plotted at various L_{rt} values (ranging from 18 μm to 207 μm) for MRRs with both straight and bent CDCs each for $\kappa_o = 2000$ m^{-1} and $\kappa_o = 8000$ m^{-1}. Plots of K_c versus L_{rt} at $\gamma = 87\%$ are shown in Figure 3.8; $\gamma = 87\%$ is used to allow for bends in the bus waveguides needed to connect to external components, and to have enough space to place heaters on top of the sections of the microring that are not covered by CDCs for thermal tuning (see section 3.3 for further discussion on the device design). For our analysis, K_c is used as a metric that is directly proportional to the to the side-mode suppression ratio (SMSR) at the MRR resonances immediately adjacent to the resonant wavelength of the filter, SMSR_{adj}. Specifically, K_c is the normalized contra-directional power coupling factor of a CDC evaluated at $\lambda_D \pm 1$FSR assuming that λ_D coincides with one of the longitudinal modes of the MRR, see Figure 3.9. In other words, $K_c = |\kappa_c(\lambda_D \pm 1FSR)|^2/|\kappa_c(\lambda_D)|^2$ where $\kappa_c(\lambda_D)$ is the field coupling factor of a CDC. From the plots in Figure 3.8, the MRRs with bent CDCs achieve larger K_c values (i.e., larger suppressions) than the MRR with straight CDCs for all plotted L_{rt} and

κ_o values. In the following section we will describe the design procedure of an MRR filter with bent CDCs.

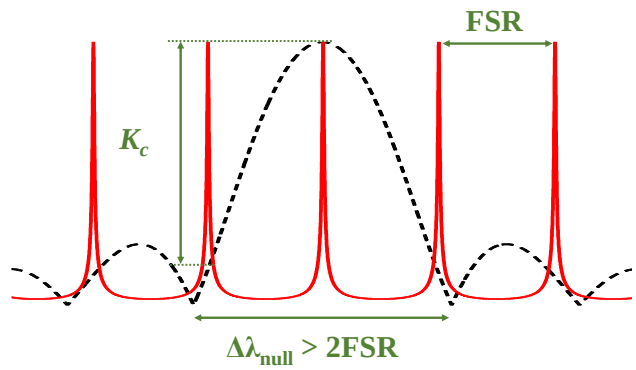

Figure 3.9: (a) A CDC's spectral response and an MRR's response when $\Delta\lambda_{null} > 2\text{FSR}$.

3.3 Device Design

Figure 3.10 shows a schematic of our proposed MRR filter with two, identical, bent CDCs. The parameters to be designed for the CDCs include W_B, W_R, ΔW_B, ΔW_R, g, and Λ, as well as the number of periods, N. The CDCs are designed so that the widths of the waveguides, W_B and W_R, are 450 nm and 550 nm, respectively; also, a ΔW_B of 30 nm and a ΔW_R of 40 nm are used [88]. Also, g = 280 nm. The widths, W_R and W_B, are asymmetric so that the wavelengths of the reflections due to the CDCs are far from the drop-port peak wavelength, λ_D, [50, 55]. λ_D is the center wavelength of the main lobes of the CDCs' drop-port spectra, and is chosen to coincide with one of the MRR's longitudinal modes in the C-band. The bent CDCs are designed using previously proposed bent coupler designs [1, 62, 89].

In order to design an MRR with bent CDCs that achieves maximum side-mode suppression, L_c of each of the CDCs, should be chosen so that it satisfies the relation in equation 3.19. Clearly, this chosen L_c value should be less than half the microring's circumference (i.e., $L_c < \pi R$) to accommodate both of the CDCs

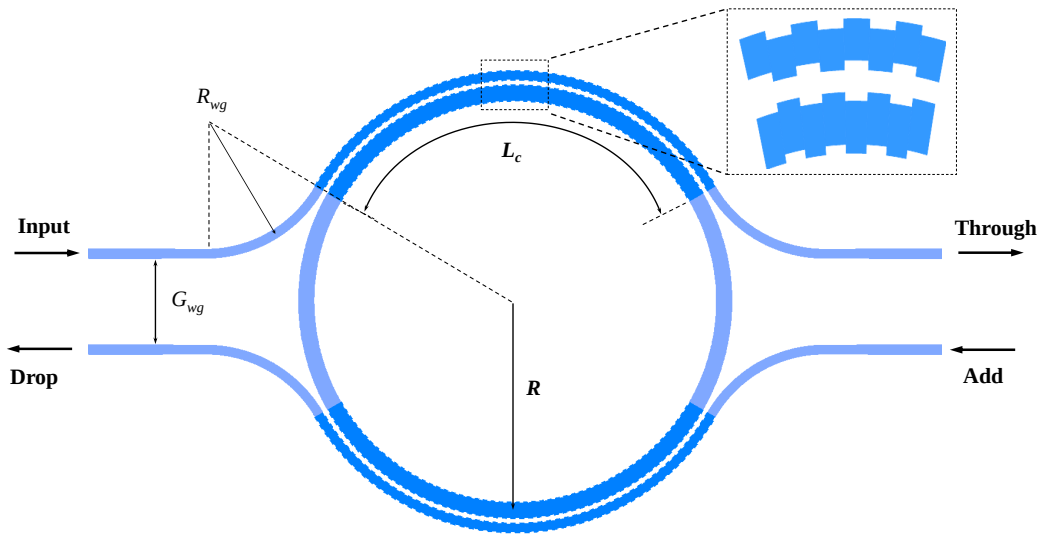

Figure 3.10: Schematic of an MRR with bent CDCs, as well as an inset showing a zoom-in of a section of a bent CDC. The dark blue traces are the corrugated waveguides (gratings) of the CDCs.

on a microring. Accordingly, R should be less than or equal to $\sim$34 µm for κ_o values up to 8000 m^{-1} (see Figure 3.11; here we used W_B = 450 nm and W_R = 550 nm). Also, it is shown in Figure 3.11 that the least possible coverage, $L_c/\pi R$, to satisfy equation 3.19 is approximately 0.964. However, such a large coverage will not allow for filter to be connected to other components (for example, the bus waveguides need bends in them of radius, R_{wg}, and to be separated from each other by G_{wg}, as illustrated in Figure 3.10). Hence, it is difficult to realize a design for which the MRR's side modes coincide exactly with the CDCs' nulls. Here, in order to minimize radiation losses in the bends we use R_{wg} = 5 µm and to minimize cross-coupling between the buses we use G_{wg} = 2.5 µm. Accordingly, L_c is chosen to accommodate our chosen R_{wg} and G_{wg} for various R values. In Figure 3.12, we have plotted the theoretical K_c, in dB, for κ_o values up to 8000 m^{-1}. As can be seen from Figure 3.12, the minimum K_c for $\kappa_o \leq$ 8000 m^{-1} and R = 34 µm is $\sim$18 dB. Nevertheless, the minimum K_c for an MRR with R = 25 µm is also $\sim$18 dB at κ_o = 8000 m^{-1}. Given that the actual fabricated κ_o will typically be less than

the simulated value, the K_c in the actual device should be greater than 18 dB for any $\kappa_o < 8000\ \mathrm{m}^{-1}$ and for R values between 25 µm and 34 µm. However, since the footprint of our device almost doubles as R changes from 25 µm to 34 µm, we have picked the smaller radius for our device.

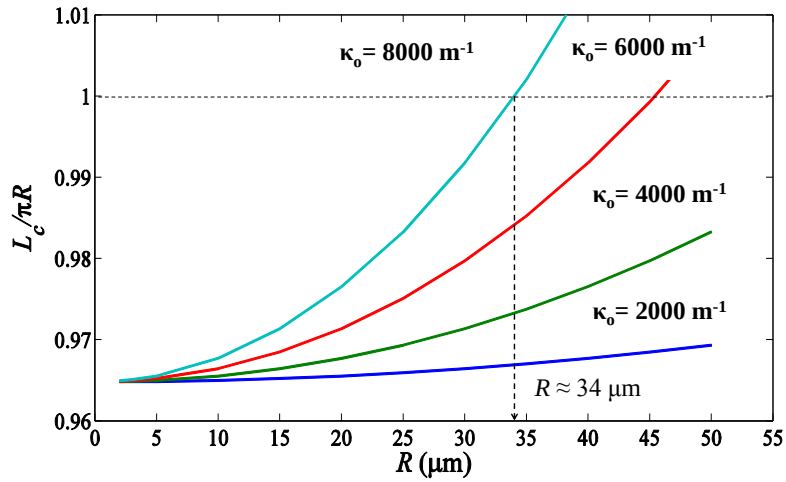

Figure 3.11: Plots of the MRR's coverage with the CDCs (Lc/πR) versus R at various κ_o values.

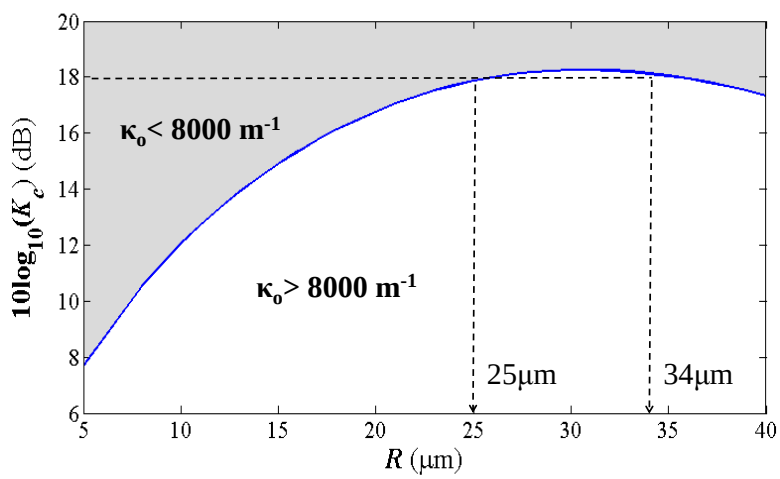

Figure 3.12: Plot of K_c, in dB, versus R at $\kappa_o = 8000\ \mathrm{m}^{-1}$.

After designing R, Λ is designed for a target λ_D value that will satisfy the phase-match condition for bent CDCs represented by equation 3.15. Hence, according to our phase-match condition, $\Lambda = 318$ nm for $\lambda_D \simeq 1537$ nm. N is chosen to be 216 to obtain maximum coverage by the CDCs, as previously discussed. Table 3.1 summarizes the design parameters for our MRR with bent CDCs. Our bent CDCs are simulated using Lumerical FDTD Solutions. Consequently, the contra-directional field coupling factor for a CDC, κ_c, and the field transmission factor, t_c, are obtained and their power factors, in dB, are shown in Figure 3.13. Also, the power coupling factor, $|\kappa_c|^2$, is fitted to equations 3.9 and 3.10 using *lsqcurvefit* function in MATLAB®; as a result, κ_o is found to be $\sim$6800 m^{-1}. The co-directional power coupling factor of the simulated bent CDC is $\sim$0.015 at 1537.2 nm (λ_D). From the CDC transmission in Figure 3.13, two notches are observed: a notch at 1537.2 nm (λ_D), due to the contra-directional coupling between the bus and ring waveguides, and a notch at $\sim$1522 nm, from intra-waveguide Bragg reflections at the input port [50].

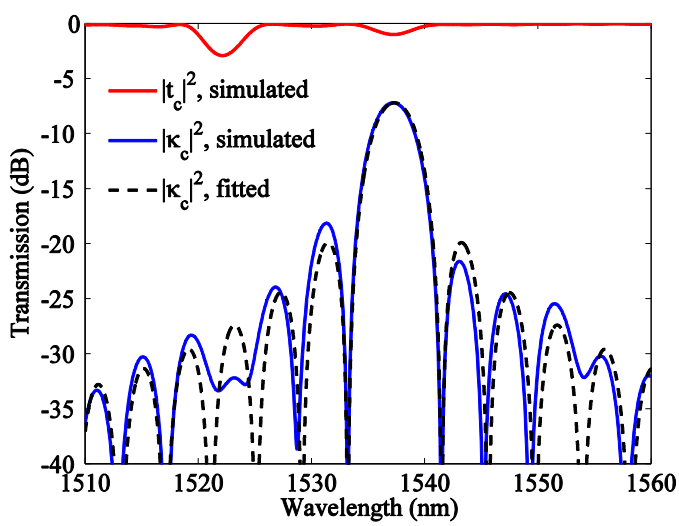

Figure 3.13: Theoretical spectral responses, for the simulated bent CDC (using FDTD), of the power transmission ($|t_c|^2$) at the through port, the power coupling ($|\kappa_c|^2$) at the drop port, as well as the fitted CDC response at the drop port.

Table 3.1: Our MRR with bent CDCs filter design parameters.

Design Parameter	Value
W_B	450 nm
W_R	550 nm
Δ_B	30 nm
Δ_R	40 nm
g	280 nm
Λ	318 nm
N	216
R	25 µm
R_{wg}	5 µm
G_{wg}	2.5 µm

3.4 MRR with Bent CDCs Transfer Function

For the contra-directional coupling, the electric field transfer function of the MRR filter with bent CDCs at the drop port, $\overline{E}_{drop}$, and at the through port, $\overline{E}_{thru}$, are derived using Mason's rule, similar to the approach presented in [90]. Mason's rule (also known as Mason's gain formula) provides a method to evaluate the transfer function between the input and output of a given system [91]. The transfer function of a system is represented by

$$G = \frac{\sum_{i=1}^{n} F_i \Delta_i}{\Delta} \tag{3.20}$$

where F_i is the gain of the ith path given that the system has n paths, and Δ=1 - (sum of all non-touching loop gains) + (sum of the products of the gains of all possible two loops that are not touching) - (sum of the products of the gains of all

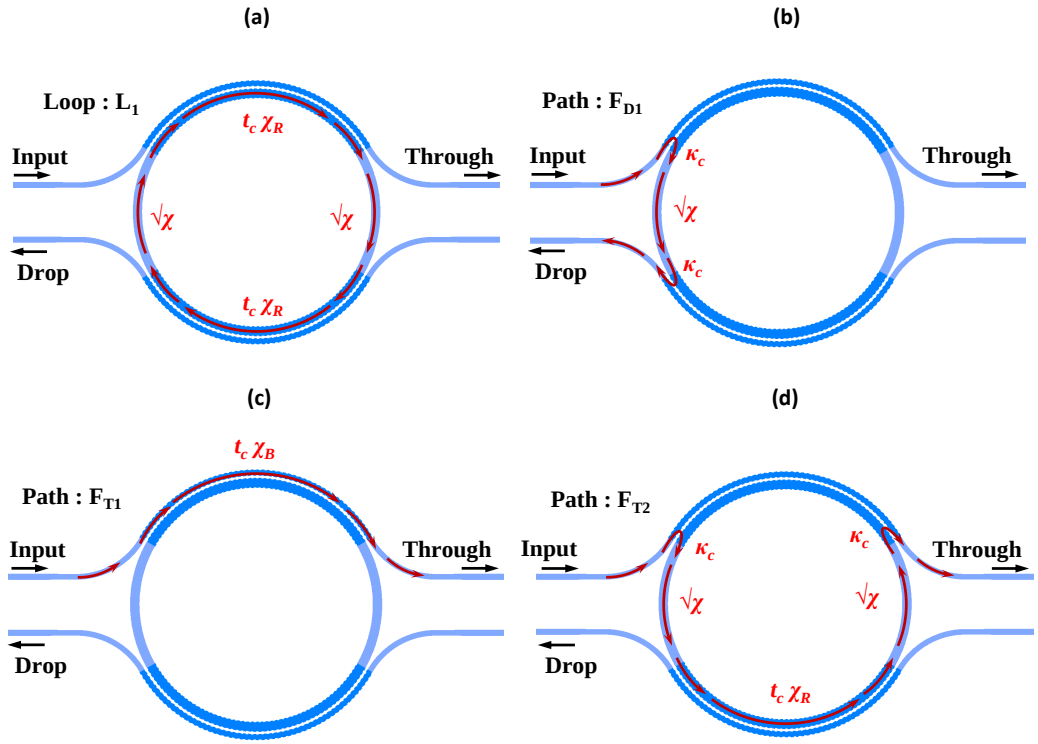

Figure 3.14: Diagrams illustrating the gains of (a) loop L_1, (b) path F_{D1}, (c) path F_{T1}, and (d) path F_{T2}.

possible three loops that that are not touching) + ... so forth. Also, Δ_i is the Δ of the loops that are not touching the ith path. Accordingly, the gain of the loop, L_1, (the loop is illustrated in Figure 3.14(a)) is given by

$$L_1 = {t_c}^2 {\chi_R}^2 \chi \tag{3.21}$$

The gain of the path for the drop-port transfer function, F_{D1}, (the path is illustrated in Figure 3.14(b)) is given by

$$F_{D1} = {\kappa_c}^2 \sqrt{\chi} \tag{3.22}$$

the gains of the first and seconds paths for the through port transfer function, F_{T1}

and F_{T2} respectively, (the paths are illustrated in Figures 3.14(c) and 3.14(d)) and are given by

$$F_{T1} = {t_c}^2 \chi_B \tag{3.23}$$

and

$$F_{T1} = {\kappa_c}^2 t_c \chi_R \chi \tag{3.24}$$

where χ, χ_B, and χ_R are the gains of the sections of the MRR that is not covered by the CDC, the bus waveguide of each of the CDCs, and the ring waveguide of each of the CDCs, respectively (their equations will be given below). Given the gain of the loops and paths of this system and following Mason's rule in equation 3.20, $\overline{E}_{drop}$ and $\overline{E}_{thru}$ are represented as

$$\overline{E}_{drop} = \frac{F_{D1}}{1 - L_1} \tag{3.25}$$

and

$$\overline{E}_{thru} = \frac{F_{T1}(1 - L_1) \ + \ F_{T2}}{1 - L_1} \tag{3.26}$$

After substituting equations 3.21 to 3.24 into equations 3.25 and 3.26, the resulting equations for $\overline{E}_{drop}$ and $\overline{E}_{thru}$ of our MRR become

$$\overline{E}_{drop} = \frac{{\kappa_c}^2 \sqrt{\chi}}{1 - {t_c}^2 {\chi_R}^2 \chi} \tag{3.27}$$

and

$$\overline{E}_{thru} = \frac{t_c \chi_B (1 - {t_c}^2 {\chi_R}^2 \chi) + {\kappa_c}^2 t_c \chi_R \chi}{1 - {t_c}^2 {\chi_R}^2 \chi} \tag{3.28}$$

where $\chi = \exp(-\frac{\alpha}{2} L - j\frac{2\pi n_R}{\lambda} L)$, $\chi_R = \exp(-\frac{\alpha}{2} L_c - j\frac{2\pi n_R}{\lambda} L_c)$, $\chi_B = \exp(-\frac{\alpha}{2} L_c - j\frac{2\pi n_B}{\lambda} L_c)$, $L_c = N \times \Lambda$, $L = 2\pi R - 2L_c$, and $\alpha/2$ is the waveguide propagation field loss in nepers per meter (i.e., α is the power loss).

3.5 Theoretical Results

Using equations 3.27 and 3.28, and assuming a propagation loss of 3 dB/cm ($\alpha \simeq 69\ m^{-1}$), the power transmission to the drop port, T_{drop}, and to the through port, T_{thru}, can be calculated. Our MRR power transmissions are calculated as, $T_{drop} = |E_{drop}|^2$ and $T_{thru} = |E_{thru}|^2$. In order to characterize the side-mode suppression of our filter using the drop-port response, we determine two side-mode suppression ratios: SMSR$_{min}$ and SMSR$_{adj}$, both of these measures are illustrated in Figure 3.15. SMSR$_{min}$ is the minimum side-mode suppression ratio within the wavelength span for which the response is measured. We use SMSR$_{min}$ to typically mean the overall SMSR of the filter. SMSR$_{adj}$ is the suppression ratio of the side modes occurring at $\lambda_D \pm$1FSR; if the suppression ratio of the side mode at λ_D+1FSR is not equal to the suppression ratio of the side mode at λ_D-1FSR, the smaller ratio is chosen to be SMSR$_{adj}$. From T_{drop}, in Figure 3.15, SMSR$_{adj}$

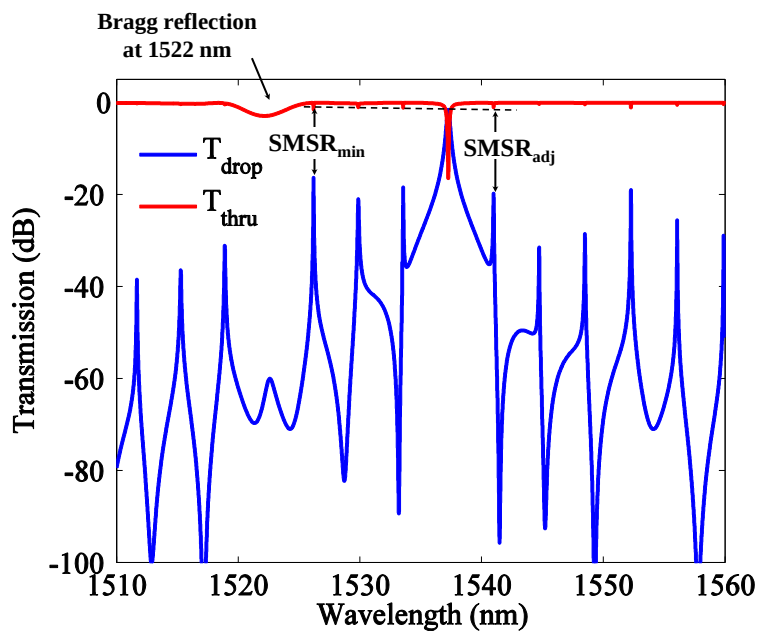

Figure 3.15: Theoretical spectral responses of our MRR filter with bent CDCs at the drop port, T_{drop}, and at through port, T_{thru}.

is 17.5 dB, which is expected given our choice of R =25 µm to achieve $K_c >$ 18 dB (as discussed above). Additionally, SMSR_{min} is ∼15 dB, the 3dB-BW is ∼35 GHz, and the insertion loss is 1.6 dB. From T_{thru}, in Figure 3.15, the ER is 16.5 dB. Furthermore, the phase of the drop-port response, ϕ_{drop}, is evaluated from $\overline{E}_{drop}$ in equation 3.27. The group delay (GD) and the chromatic dispersion (CD) are then calculated using the following equations.

$$GD = \frac{\phi_{drop}}{2\pi f} \tag{3.29}$$

and

$$CD = \frac{GD}{\lambda} \tag{3.30}$$

The resulting group delay and chromatic dispersion of our MRR filter are shown in Figures 3.16(a) and 3.16(b). The drop-port chromatic dispersion within a 25 GHz window around 1537.2 nm, is ±42 ps/nm.

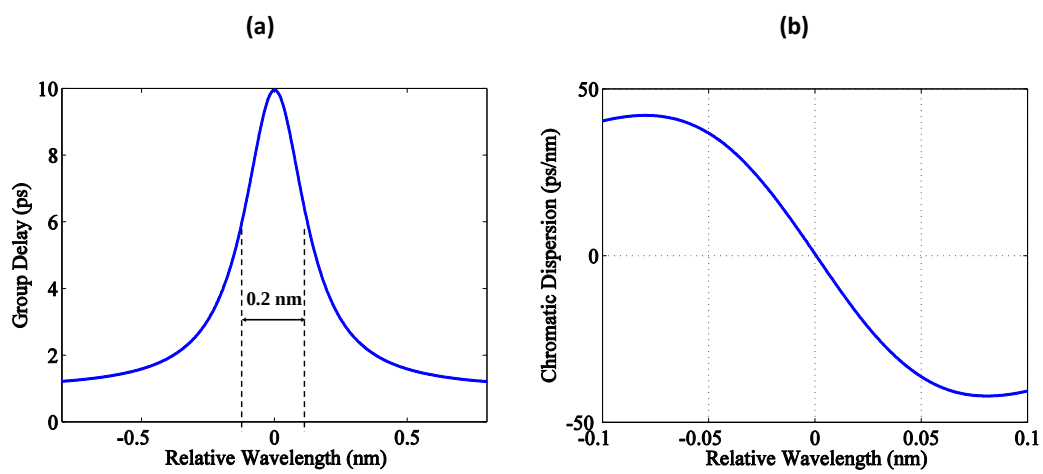

Figure 3.16: The (a) group delay (GD) and (b) chromatic dispersion (CD) at the drop-port around 1537.2 nm.

3.6 Device Fabrication

The MRR filter with bent CDCs was fabricated using electron beam lithography at the University of Washington [92]. The fabricated device has strip waveguides with 220 nm heights and a top oxide cladding. Metal heaters are used on top of the MRR waveguides for thermal tuning. A total of three sections of micro-heaters are used: two sections on top of the CDCs and another section on top of portions of the microring that don't contain gratings, and each of the heater sections is tuned separately. A microscopic image of our fabricated MRR filter is shown in Figure 3.17. GC structures are also used to couple TE modes into and out of the device for measurements purposes [93].

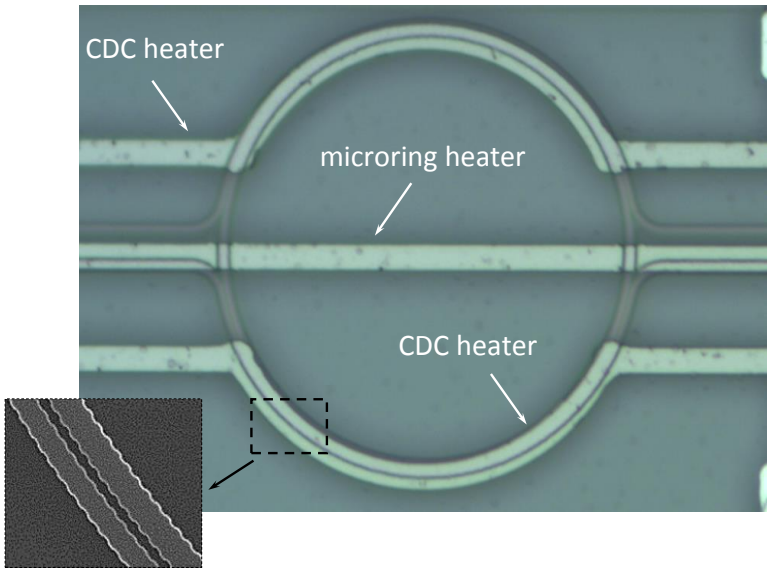

Figure 3.17: A microscopic image of our MRR filter with metal heaters; the inset shows a scanning electron microscope (SEM) image of a portion of a bent CDC.

3.7 Measurement Results

The spectral responses at both the drop and through ports are shown in Figure 3.18(a) for wavelengths between 1520 nm and 1580 nm. These responses include the responses of the GCs at the input (input port) and the outputs (drop port and/or through port). The setup used to measure the optical spectra of our filter include an Agilent 81682A sweepable laser source and an Agilent 81635A optical power meter; both of these are used in an an Agilent 8164A mainframe. In these measurements, the laser source, with a 0 dBm optical power, sweeps the output wavelength between 1520 nm and 1580 nm at equally spaced wavelength steps and the optical power meter measures the output power at each of the wavelength steps. A Python script is then used to plot the relative output power versus the laser wavelengths to get the responses shown in Figure 3.18(a). The drop-port spectral response shows a single resonant peak at ∼1540.3 nm in a 60 nm wavelength span, which contains the C-band. In addition, the SMSR_{adj} is 20.7 dB and the SMSR_{min} is more than 15 dB. Additionally, from the normalized responses (i.e., where the

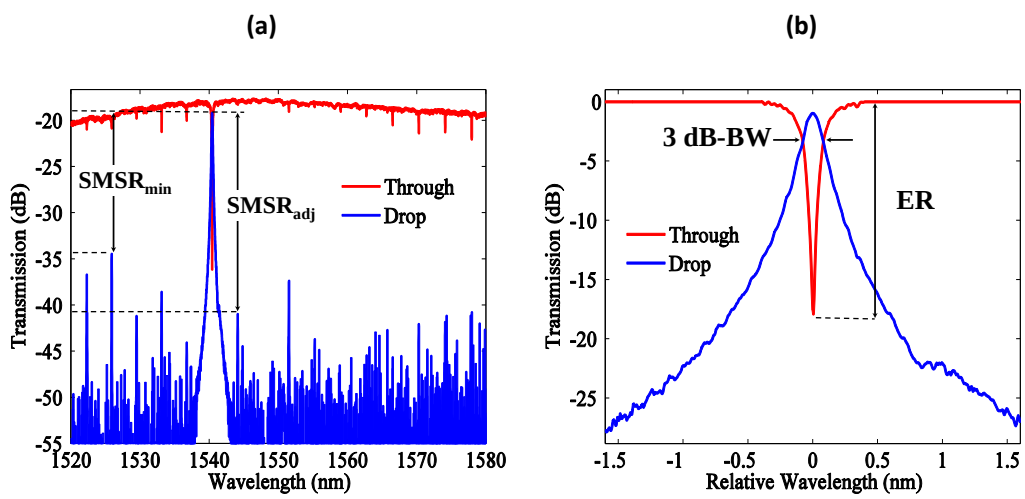

Figure 3.18: (a) Spectral responses of our MRR filter at the drop and through ports; the illustrated SMSR is 15.3 dB. (b) The responses relative to 1540.3 nm, after normalizing them with respect to the grating couplers' responses.

grating couplers' responses have been de-embedded) in Figure 3.18(b), the ER is ∼18 dB, the 3dB-BW is ∼23 GHz, and the drop-port insertion loss (IL_{drop}) is ∼1 dB. Furthermore, the suppressed notch at the through port, at 1533.1 nm, has a magnitude of 2.9 dB. The drop-port response is measured at various total tuning powers for both heater sections, and the responses are shown in Figure 3.19(a). In these measurements, power is applied to the CDC heaters to shift the drop-port peak wavelength, while power is applied to the microring heater to align the microring's response with the CDCs' responses. Our MRR filter with bent CDCs demonstrates tunability with a tuning efficiency, η, of ∼56 mW/nm, as shown in Figure 3.19(b). The chromatic dispersion at the filter's drop-port is measured using a Luna Optical Vector Analyzer™. From Figure 3.20, the chromatic dispersion within a 25 GHz window centered on 1540.3 nm is ±90 ps/nm.

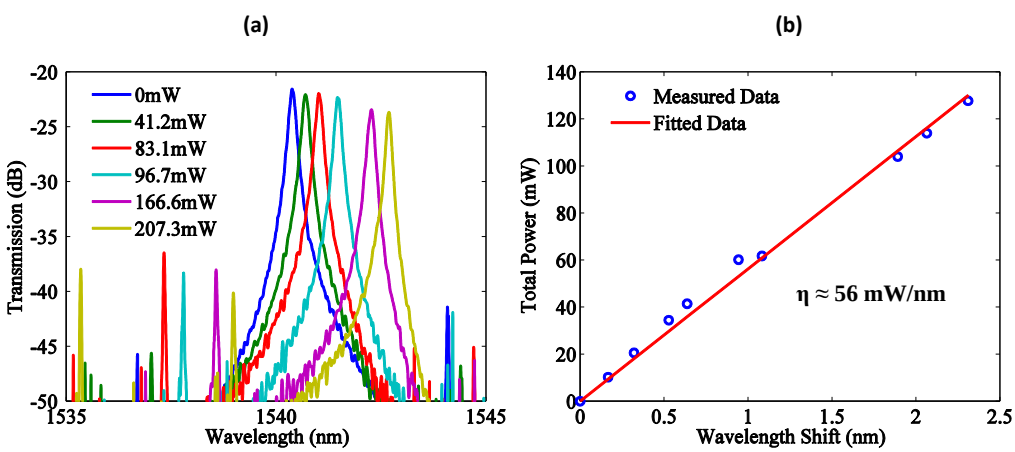

Figure 3.19: (a) Drop-port responses at various total tuning powers. (b) Plot of the total tuning power versus wavelength shift.

3.8 Discussion

Table 3.2 gives a comparison between the as-designed results (obtained in section 3.5) and the measured results of our filter. Clearly, the measured dispersion is larger than the as-designed value because the κ_o of the fabricated device is less

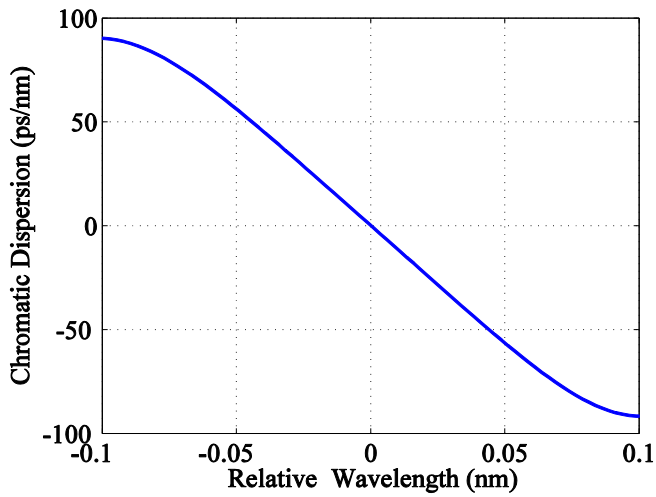

Figure 3.20: Chromatic dispersion at the drop port in a 25 GHz window relative to 1540.3 nm.

than that of the simulated device. This would be consistent with the reduction in the 3dB-BW and the increase in SMSR_{adj} from the design value. The measured drop-port response is thus fitted to obtain κ_o and α of our fabricated filter. Our objective is to verify the model that we use to obtain the theoretical responses for MRRs with bent CDCs and to verify that κ_o of the fabricated device is less than our design value of 6800 m^{-1}. Here, we fit the measured drop-port response to the magnitude-squared of equation 3.27, and κ_c and t_c are obtained using the CDC's coupled-mode equations described in section 3.1. From our fit, κ_o is found to be 5530 m^{-1} and α is found to be $\sim$161 m^{-1} (i.e., a power propagation loss of 7 dB/cm). Clearly, κ_o of the fabricated device is smaller than the design value and α of the fabricated device is larger than the design value. $\overline{E}_{drop}$ and $\overline{E}_{thru}$ are then recalculated using equations 3.27 and 3.28 and using the fitted κ_o and α values. The magnitude-squared response of the calculated $\overline{E}_{drop}$ (fitted response), and the measured and theoretical (designed) drop-port responses are shown in Figure 3.21; the fitted response shows a closer agreement to the measured response as compared to the designed response. The following are the extracted results

Table 3.2: Summary of the as-designed, measured, and fitted results of our MRR filter with bent CDCs and its comparison with the results of a previously demonstrated MRR with straight CDCs.

Parameter	This device (Designed)	This device (Measured)	This device (Fitted)	Shi *et al.* [55]
Footprint (μm^2)	1963	1963	1963	6880
λ_r (nm) [1]	1537.2	1540.3	1540.3	1504.6
κ_o (m^{-1})	6800	5530	5530	2000
$SMSR_{min}$ (dB)	15	>15	19.2	> 8
$SMSR_{adj}$ (dB)	17.5	>20.7	19.2	> 8
ER (dB)	16.5	∼18	22.8	> 10
3dB-BW (nm)	0.28	0.18	0.19	0.06
IL_{drop} (dB)	1.6	∼1	0.7	N/A
Dispersion (ps/nm)	±42	±90	±90	N/A

[1] λ_r is the MRR filter's resonant wavelength

from the calculated $\overline{E}_{drop}$ and $\overline{E}_{thru}$ responses: $SMSR_{adj}$ = 19.2 dB, IL_{drop} = 0.7 dB, 3dB-BW = 24 GHz (0.19 nm), and ER = 22.8‘dB. These results closely agree with the measured results, see Table 3.2. Also, the chromatic dispersion within a 25 GHz window centered on 1540.3 nm is ±90 ps/nm; this dispersion matches the measured dispersion, see Table 3.2. We can thus safely conclude that our model closely approximates the fabricated device and that the assumptions we made during our design procedure (such as co-directional coupling is negligible) are valid.

Table 3.2 also gives a comparison between the measured results of our filter

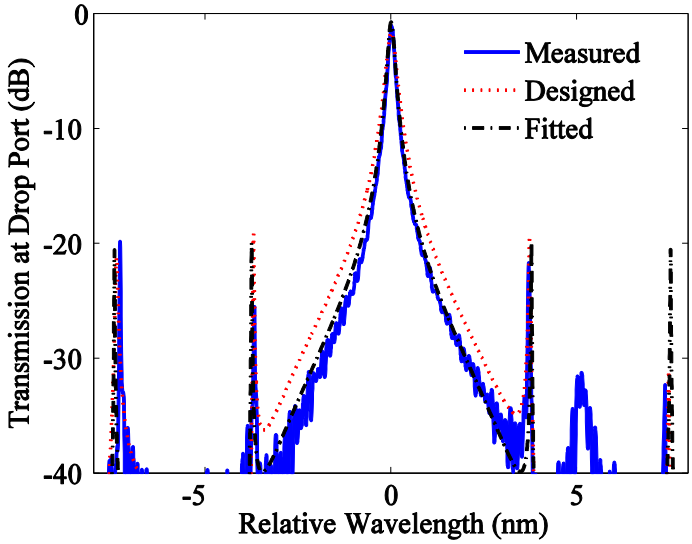

Figure 3.21: Drop-port spectral responses from the measured data and from $\overline{E}_{drop}$ calculated using fitted κ_o and α values relative to 1540.3 nm, as well as the theoretical drop-port response obtained in section 3.5 relative to 1537.2 nm.

and previously reported values for a single-ring MRR with straight CDCs [55]. Our MRR filter achieves larger SMSR_{adj} and SMSR_{min} than those of the previously demonstrated MRR filter with straight CDCs even though κ_o of our filter is larger. In addition, our MRR filter with bent CDCs has a footprint of $\sim$1963 μm^2, which is significantly more compact, less than one-third the area, as compared to the previously demonstrated MRR with straight CDCs. In section 3.2, we have shown that an MRR with bent CDCs will achieve larger side-mode suppressions than an equivalent MRR with straight CDCs, see Figure 3.8. As a result, we designed our proof-of-concept MRR with bent CDCs so as to achieve higher side-mode suppressions and to be more compact than other demonstrated MRRs with straight CDCs. Our proof-of-concept filter achieved our predicted design results and demonstrated a more attractive alternative to MRRs with straight CDCs that has higher suppressions and is more space-efficient while still having the advantages of integrating CDCs in the coupling regions.

3.9 High-Speed Testing

In order to characterize the demonstrated filter for high-speed data transmission, an experimental setup is used similar to the one proposed in [94]. Our experimental setup is shown in Figure 3.22 and Table 3.3 lists the equipment used in the setup. Our setup is composed of a tunable laser source (TLS), a pulse pattern generator (PPG), a Mach-Zehnder modulator (MZM), an erbium-doped fiber amplifier (EDFA), a variable optical attenuator (VOA), an optical tunable filter (OTF), a photo-detector (PD), and a digital communication analyzer (DCA). The EDFA and the attenuator together provide variable gain at the output of our filter. The total gain of this stage is set so that the peak power of the data at the PD is 0 dBm. The MZM has polarization maintaining input and output fibers. The OTF wavelength is set to be the same as the TLS wavelength, and the bandwidth of the OTF is set to be 2 nm. NRZ signals with $2^{31} - 1$ PRBS patterns and data rates of 12.5 Gbps, 20 Gbps, and 28 Gbps are used in our characterizations.

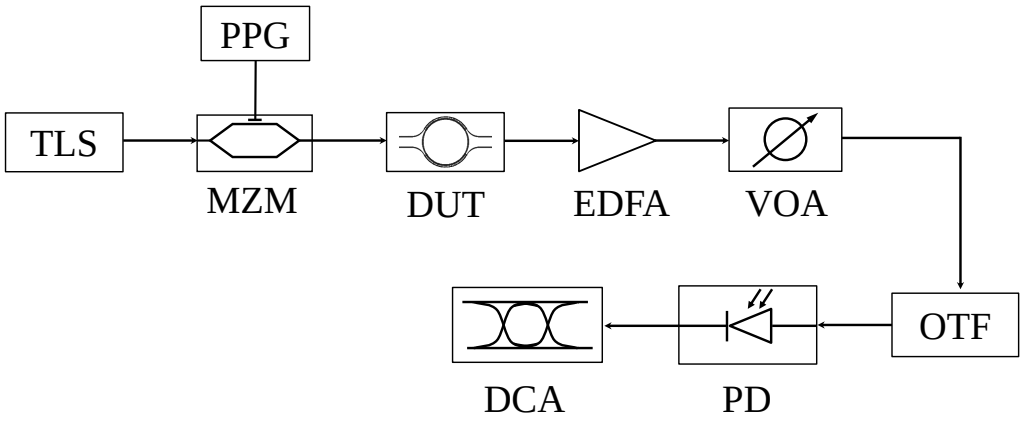

Figure 3.22: Block diagram showing the experimental setup used to measure the eye diagrams of our filter

Eye diagrams of the modulated NRZ data are measured at the input and at the drop port of our filter at 1540.3 nm for data rates of 12.5 Gbps, 20 Gbps, and 28 Gbps, see Figures 3.23(a)-3.23(f). A wavelength of 1540.3 nm corresponds to the center wavelength of our filter. Here, the signal at the input to our filter is

Table 3.3: List of equipment used in our setup to measure the eye diagrams and BERs of our MRR filter.

Instrument	Equipment Model
TLS	Keysight N7714A
PPG	Anritsu MP1800A BERT (PPG module)
MZM	$LiNb0_3$ Lucent X2623Y
EDFA	Fiberprime EDFA-C-26G-S
VOA	HP 8156A
OTF	Santec OTF-950
PD	Lab Buddy DSC-R411
DCA	Agilent 86100A
BERT	Anritsu MP1800A

the signal from the MZM. As can be seen from Figures 3.23(a)-3.23(f), the eyes exhibit small reductions in the signal quality at the drop port of our filter. We are also interested in the data transmitted at the through port for wavelengths that are not being filtered. Specifically, eye diagrams are measured at the input and at the through port of our filter at 1533.1 nm, which corresponds to the major suppressed notch. The major suppressed notch was chosen because it is the point at which the largest deterioration of the signal is expected [95]. The eye diagrams are shown in Figures. 3.23(g)-3.23(i) at the input to our filter and in Figures 3.23(j)-3.23(l) at the through port of our filter. The patterns maintain open eyes at the through port's notch at 1533.1 nm for data rates up to 28 Gbps with minimal reduction in the signal quality.

Our filter is further characterized for high-speed data transmission by measuring its bit error rate (BER). The experimental setup used to measure the BER is

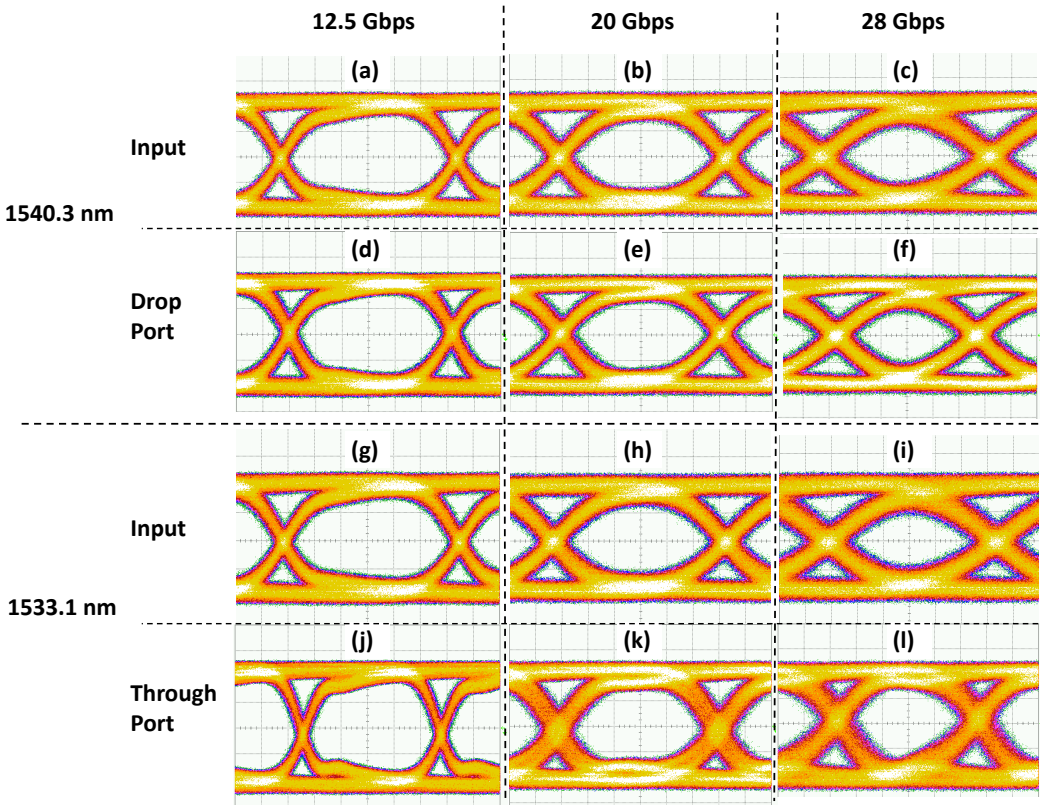

Figure 3.23: Eye diagrams of NRZ data at the input of our filter at 1540.3 nm for data rates of (a) 12.5 Gbps, (b) 20 Gbps, and (c) 28 Gbps as well as at the drop port (output) for data rates of (d) 12.5 Gbps, (e) 20 Gbps, and (f) 28 Gbps. Eye diagrams of NRZ data at 1533.1 nm at the input of our filter for data rates of (g) 12.5 Gbps, (h) 20 Gbps, and (i) 28 Gbps as well as at the through port (output) for data rates of (j) 12.5 Gbps, (k) 20 Gbps, and (l) 28 Gbps.

shown in Figure 3.24. The setup is similar to the one used to measure the eye diagram. However, in this setup (to measure the BER) the output of the PD is fed to the error detection (ED) module of the bit error rate tester (BERT). Also, the received power is varied at the PD by varying the attenuation setting of the VOA. BERs of the modulated NRZ data (2^{31}-1 PRBS pattern) are measured at the drop port of our filter at 1540.3 nm for data rates of 12.5 Gbps, 20 Gbps, and 25 Gbps. Also, BERs are measured at the through port of our filter at 1533.1 nm for data rates of 12.5 Gbps, 20 Gbps, and 25 Gbps. The BER plots versus the received optical power at the PD are shown in Figure 3.25. A BER below 10^{-12} is taken to mean than the transmission of the data is essentially error free. Accordingly, at a received optical power of 1.5 dBm, error-free transmission is achieved at the through port for data rates up to 25 Gbps and at the drop port for data rates up to 20 Gbps. However, at a received power of 4 dBm, error-free transmission is achieved for the drop and through ports for data rates up to 25 Gbps. In general, the data at the through port has lower BERs, at the various received powers, as compared to data at the drop port, and both ports can have error-free transmission for data rates up to 25 Gbps.

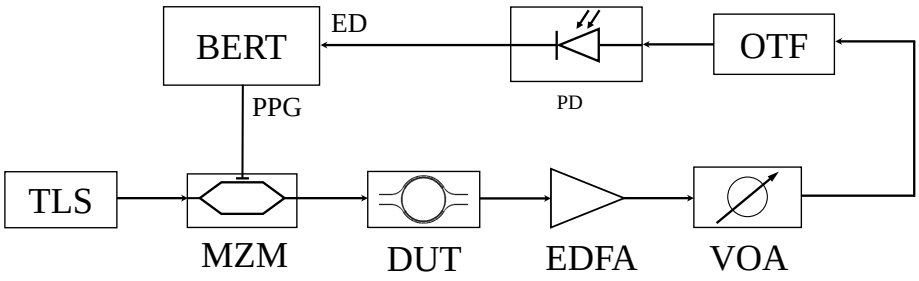

Figure 3.24: Diagram showing the experimental setup used to measure the BER of our filter.

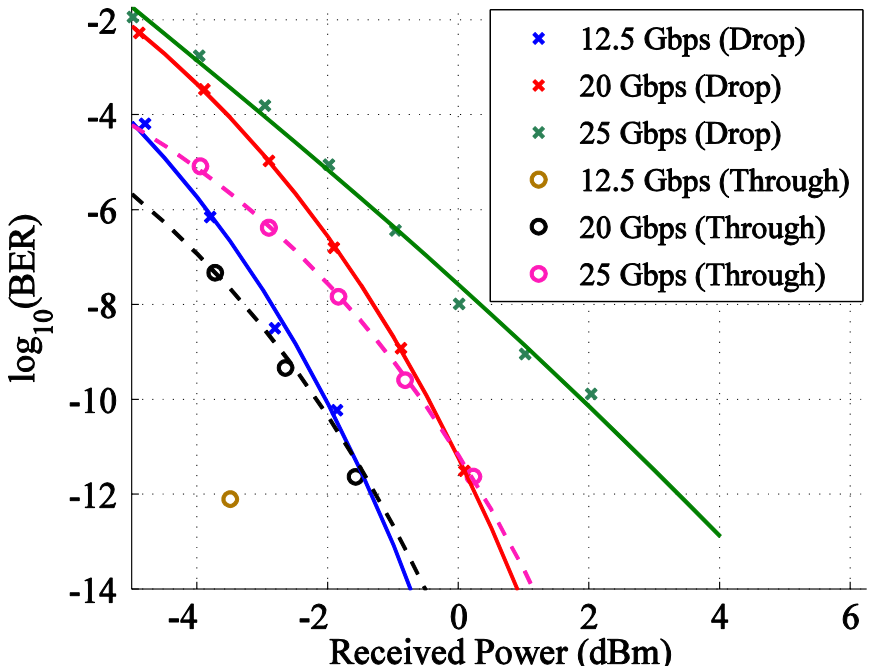

Figure 3.25: Measured BERs versus received optical power at the PD at data rates of 12.5 Gb/s, 20 Gb/s, and 25 Gb/s at the drop port, at 1540.3 nm, and at the through port, at 1533.1 nm.

3.10 Summary

In conclusion, we study the design of an SOI MRR based filter with bent CDCs in which the CDCs are partially wrapped around the MRR. With the aid of bending the CDCs, a relatively compact filter design with an FSR-free response, a relatively high SMSR, and a large 3dB-BW is achieved. Our design facilitates the use of MRR based multiplexers/de-multiplexers for densely integrated optical interconnects in WDM systems, where large channel capacities and small chip footprints are desired. The fabricated MRR filter with bent CDCs is experimentally demonstrated showing an FSR-free response at both the drop port and the through port. Moreover, the measurements show an $SMSR_{min}$ of more than 15 dB; such an SMSR would be difficult to obtain using MRRs with straight CDCs. Also, our

filter has a 3dB-BW of $\sim$23 GHz and has an ER of $\sim$18 dB. The eye diagrams of NRZ $2^{31} - 1$ PRBS patterns, for data rates up to 28 Gbps, exhibit small reductions in the signal quality at the drop port and the through port of our filter.

Chapter 4

Summary, Conclusions, and Suggestions for Future Work

4.1 Summary and Conclusions

In this research, we demonstrated MRR filters that used bent couplers in their coupling regions. We first studied and experimentally demonstrated an MRR filter that used bent directional couplers in Chapter 2. By using bent directional couplers, we were able to fabricate a 2.75 um radius MRR filter using a 248 nm photolithography process and to achieve our desired performance. Because of the bent couplers, our MRR filter had a wide FSR of 33.4 nm (covering most of the C-band) and sufficient coupling to achieve a wide 3dB-BW of 25 GHz, a large OBRR of 42 dB, a large ER of 19 dB, and an IL_{drop} of less than 1 dB. Additionally, our MRR had metal heaters on top of it for thermal tuning as well as air trenches around it and silicon undercuts to achieve an improved thermal efficiency of 12 mW/FSR. In Chapter 3, we experimentally demonstrated a novel design of an MRR filter with bent CDCs. By using CDCs in the coupling regions of an MRR filter, FSR-free responses at the drop port and the through port are achieved. In addition, by bending the CDCs around the MRR, a large side-mode suppression can be achieved. Also, our MRR with bent CDCs achieved

a more compact filter design as compared to the previously demonstrated MRR with straight CDCs. Our MRR filter achieved a larger $SMSR_{min}$ of more than 15 dB, a 3dB-BW of $\sim$23 GHz, and an ER of $\sim$18 dB. Our MRR filter was also demonstrated for high-speed transmission of NRZ data, $2^{31} - 1$ PRBS patterns. This high-speed testing was performed by measuring the eye diagrams at the input port, the drop port, and the through port of our filter for data rates up to 28 Gbps, and by measuring the BER at the drop port and the through port for data rates up to 25 Gbps. The drop-port measurements were performed at the resonant wavelength, and the through-port measurements were performed at the wavelength of the major (in magnitude) suppressed notch. From these measurements, open eyes were achieved for the transmissions with minimal reductions in the signal quality between the input and the drop ports, as well as between the input and the through ports. Error-free (BER $< 10^{-12}$) transmissions were also observed, for the drop and the through ports, at a received optical power (after amplification) of 0 dBm.

Additionally, in Chapter 3 we showed that it is not possible to realize designs for MRR filters with straight CDCs such that the microrings' side modes coincide with the nulls of the CDCs' responses, and, as a result, MRR filters with straight CDCs cannot achieve maximum (i.e., complete) side-mode suppressions, see Figure 3.7. Nevertheless, in MRR filters with bent CDCs, it is possible to realize designs for which maximum side-mode suppressions can be achieved, see Figure 3.7. In our proof-of-concept MRR with bent CDCs we were not able to attain a design that had the γ (CDC coverage of the microring) value required to achieve maximum suppression. While there were additional considerations related to attaching the bus waveguides to the CDCs, the primarily reason we could not achieve the required γ value was that we used two identical CDCs (in both of the coupling regions) in our design. This was because we wanted to keep our design similar to the MRR filter with straight CDC for comparison purposes. After obtaining the additional insights into this issue as a result of our work, we conclude that it should be possible to achieve maximum suppressions if a CDC was used in one of the coupling regions while the other coupling region used a direc-

tional coupler. In this case, the CDC coverage requirements will be lessened, γ will be halved. When we were trying to obtain maximum suppression for an MRR having two identical CDCs in its coupling regions, γ values between $\sim$96% (for κ_o = 2000 m^{-1}) and $\sim$98% (for κ_o = 8000 m^{-1}) were required for R = 25 um. Therefore, if an otherwise identical MRR had one CDC in one of its coupling regions then the γ values would be reduced to $\sim$48% (for κ_o = 2000 m^{-1}) and $\sim$49% (for κ_o = 8000 m^{-1}). These new γ values, when a CDC is used in one of the MRR's coupling regions, are less than 50% and, thus, can be achieved while having sufficient room to attach the bus waveguides to the filter. In addition to achieving the maximum possible suppression, such a design will have better tuning efficiency. This is because, in this proposed design, only one CDC needs tuning and the portion of the microring that is not covered by the CDC is increased. This means that one CDC heater is used, which decreases power consumption, and that a larger microring heater can be used, which increases thermal efficiency. In the next section, we will discuss, and give some suggested designs that use a CDC in only one of the MRR's coupling regions, as well as give some suggested designs that utilize bent directional couplers.

4.2 Suggestions for Future Work

In this thesis, we demonstrate two MRR filter designs in which bent couplers are used to improve their performance. Another possible application of utilizing bent couplers in MRR filters could be by using them in the coupling regions of series-coupled Vernier ring filters. By doing this one can realize MRR filters that have FSRs exceeding the span of the C-band and have compact footprints. Additionally, bent couplers allow for the MRRs to have the desired coupling coefficients to achieve wide bandwidths and large ERs. As a result, these Vernier ring filters with bent couplers can have wide FSRs, have wide 3dB-BWs, and have small footprints. In Figures 4.1(a) and 4.1(b) we show two possible designs for Vernier ring filters with bent directional couplers. In the design shown in Figure 4.1(a), the ring waveguide' widths are adiabatically tapered such that the widths of the

ring waveguides at gap_2 are smaller than the widths of the ring waveguides at gap_1 and gap_3. This is done to increase the coupling coefficient of the coupler at gap_2 to achieve the desired performance. In the design shown in Figure 4.1(b), which uses a bent directional coupler at the coupler between the microrings (at gap_2), one of the microrings is slightly deformed from the typical ring shape to allow for the bent directional coupler. Such a design has a more compact footprint as compared to the design shown in Figure 4.1(a).

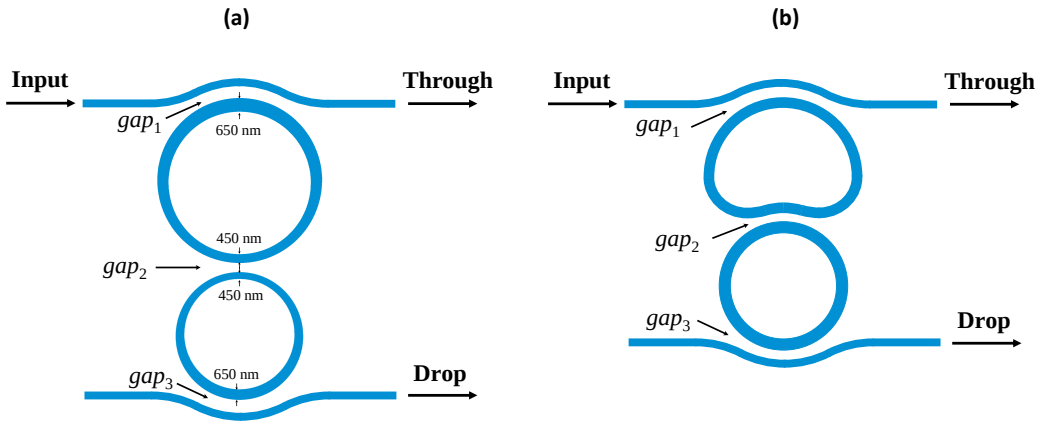

Figure 4.1: (a) A schematic of a proposed two series-coupled Vernier ring filter with bent directional couplers in their bus to ring coupling regions and adiabatic tapering of the widths of the waveguides of the microrings. (b) A schematic of a proposed two series-coupled Vernier ring filter with bent directional couplers in all of its coupling regions.

In our proof-of-concept MRR with bent CDCs, the measured SMSR at the side modes adjacent to the filter's resonance was ∼20 dB. Although this SMSR was sufficient to obtain an FSR-free response, a larger SMSR can be achieved if changes are made to the design that make the microring longitudinal side modes align with the CDC's nulls. As has been discussed in section 4.1, the MRR filter can be designed such that it uses bent CDCs in one of its coupling regions and a directional coupler at the other coupling region. However, in order to achieve a low IL_{drop}, a wide 3dB-BW, and a large ER, as in our demonstrated proof-of-concept MRR filter with bent CDCs, the coupling coefficients of both couplers should be

matched at the filter's resonance. Because of fabrication errors, the coupling coefficient of the fabricated coupler will likely be different from the simulated one and, thus, the coupling coefficients of both couplers of the fabricated filter will, typically, not be matched. This issue can be solved by using a tunable MZI as the directional coupler, see Figure 4.2; this will allow one to tune the coupling coefficient so that it matches the CDC's coupling and, thus, provide extra flexibility. Tuning of the MZI and the CDC are typically done using metal heaters.

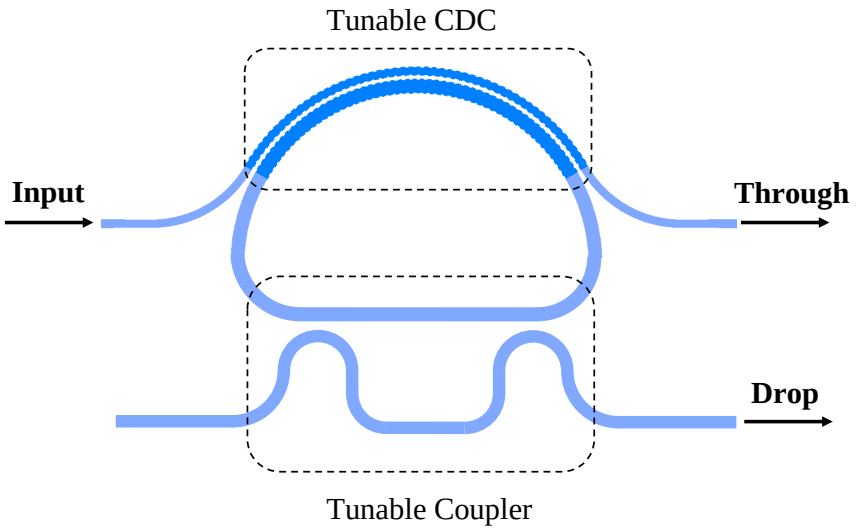

Figure 4.2: A schematic of an MRR with bent CDC in one of its coupling regions and a tunable directional coupler in the other coupling region.

Bibliography

[1] N. Eid, H. Jayatilleka, M. Caverley, S. Shekhar, L. Chrostowski, and N. A. F. Jaeger, "Wide FSR silicon-on-insulator microring resonator with bent couplers," in *IEEE 12th International Conference on Group IV Photonics*. IEEE, Aug. 2015, pp. 96–97.

[2] S. J. B. Yoo, "Future prospects of silicon photonics in next generation communication and computing systems," *Electronics Letters*, vol. 45, no. 12, pp. 584–588, June 2009.

[3] Y. A. Vlasov, "Silicon cmos-integrated nano-photonics for computer and data communications beyond 100g," *IEEE Communications Magazine*, vol. 50, no. 2, pp. s67–s72, Feb. 2012.

[4] M. A. Popovic, M. T. Wade, J. S. Orcutt, J. M. Shainline, C. Sun, M. Georgas, B. Moss, R. Kumar, L. Alloatti, F. Pavanello, Y.-H. Chen, K. Nammari, J. Notaros, A. Atabaki, J. Leu, V. Stojanovic, and R. J. Ram, "Monolithic silicon photonics in a sub-100nm SOI CMOS microprocessor foundry: progress from devices to systems," vol. 9367, 2015, pp. 93 670M–93 670M–10.

[5] T. Y. Liow, K. W. Ang, Q. Fang, J. F. Song, Y. Z. Xiong, M. B. Yu, G. Q. Lo, and D. L. Kwong, "Silicon modulators and germanium photodetectors on SOI: Monolithic integration, compatibility, and performance optimization," *IEEE Journal of Selected Topics in Quantum Electronics*, vol. 16, no. 1, pp. 307–315, Jan. 2010.

[6] M. R. Reshotko, D. L. Kencke, and B. Block, "High-speed CMOS-compatible photodetectors for optical interconnects," vol. 5564, 2004, pp. 146–155.

[7] G. T. Reed, G. Mashanovich, F. Y. Gardes, and D. J. Thomson, "Silicon optical modulators," *Nature Photonics*, vol. 4, pp. 518–526, Aug. 2010.

[8] W. Bogaerts, S. K. Selvaraja, P. Dumon, J. Brouckaert, K. D. Vos, D. V. Thourhout, and R. Baets, "Silicon-on-insulator spectral filters fabricated with CMOS technology," *IEEE Journal of Selected Topics in Quantum Electronics*, vol. 16, no. 1, pp. 33–44, Jan. 2010.

[9] B. B. Bakir, A. V. de Gyves, R. Orobtchouk, P. Lyan, C. Porzier, A. Roman, and J. M. Fedeli, "Low-loss (¡ 1 db) and polarization-insensitive edge fiber couplers fabricated on 200-mm silicon-on-insulator wafers," *IEEE Photonics Technology Letters*, vol. 22, no. 11, pp. 739–741, June 2010.

[10] Y. Tang, Z. Wang, L. Wosinski, U. Westergren, and S. He, "Highly efficient nonuniform grating coupler for silicon-on-insulator nanophotonic circuits," *Optics Letters*, vol. 35, no. 8, pp. 1290–1292, Apr. 2010.

[11] W. D. Sacher, T. Barwicz, B. J. F. Taylor, and J. K. S. Poon, "Polarization rotator-splitters in standard active silicon photonics platforms," *Optics Express*, vol. 22, no. 4, pp. 3777–3786, Feb. 2014.

[12] G. E. Keiser, "A review of WDM technology and applications," *Optical Fiber Technology*, vol. 5, no. 1, pp. 3 – 39, 1999.

[13] X. Zheng and A. V. Krishnamoorthy, "A WDM CMOS photonic platform for chip-to-chip optical interconnects," in *2014 Conference on Lasers and Electro-Optics (CLEO) - Laser Science to Photonic Applications*, June 2014, pp. 1–2.

[14] "Data center interconnect market trends and requirements," Alcatel-Lucent, Tech. Rep., 2014.

[15] A. Liu, L. Liao, Y. Chetrit, J. Basak, H. Nguyen, D. Rubin, and M. Paniccia, "Wavelength division multiplexing based photonic integrated circuits on silicon-on-insulator platform," *IEEE Journal of Selected Topics in Quantum Electronics*, vol. 16, no. 1, pp. 23–32, Jan. 2010.

[16] A. O. Networking. WDM. (Date Accessed: August 2016). [Online]. Available: http://www.advaoptical.com/en/products/technology/wdm.aspx

[17] P. P. Absil, P. Verheyen, P. D. Heyn, M. Pantouvaki, G. Lepage, J. D. Coster, and J. V. Campenhout, "Silicon photonics integrated circuits: a manufacturing platform for high density, low power optical I/O's," *Optics Express*, vol. 23, no. 7, pp. 9369–9378, Apr. 2015.

[18] "CWDM and DWDM: Wavelength guide," smartoptics, Tech. Rep.

[19] C. Corportation. DWDM vs. CWDM. (Date Accessed: August 2016). [Online]. Available: http://www.ciena.com/technology/dwdm-vs-cwdm/

[20] T. Baehr-Jones, R. Ding, Y. Liu, A. Ayazi, T. Pinguet, N. C. Harris, M. Streshinsky, P. Lee, Y. Zhang, A. E.-J. Lim, T.-Y. Liow, S. H.-G. Teo, G.-Q. Lo, and M. Hochberg, "Ultralow drive voltage silicon traveling-wave modulator," *Optics Express*, vol. 20, no. 11, pp. 12 014–12 020, May 2012.

[21] P. Dong, L. Chen, and Y. kai Chen, "High-speed low-voltage single-drive push-pull silicon Mach-Zehnder modulators," *Optics Express*, vol. 20, no. 6, pp. 6163–6169, Mar. 2012.

[22] S. Gupta, S. A. Srinivasan, M. Pantouvaki, H. Chen, P. Verheyen, G. Lepage, D. V. Thourhout, G. Roelkens, K. Saraswat, P. Absil, and J. V. Campenhout, "50 GHz ge waveguide electro-absorption modulator integrated in a 220 nm SOI photonics platform," in *Optical Fiber Communication Conference*. Optical Society of America, 2015.

[23] Y. Tang, H.-W. Chen, S. Jain, J. D. Peters, U. Westergren, and J. E. Bowers, "50 Gb/s hybrid silicon traveling-wave electroabsorption modulator," *Optics Express*, vol. 19, no. 7, pp. 5811–5816, Mar. 2011.

[24] G. Li, A. V. Krishnamoorthy, I. Shubin, J. Yao, Y. Luo, H. Thacker, X. Zheng, K. Raj, and J. E. Cunningham, "Ring resonator modulators in silicon for interchip photonic links," *IEEE Journal of Selected Topics in Quantum Electronics*, vol. 19, no. 6, pp. 95–113, Nov. 2013.

[25] S. Manipatruni, L. Chen, and M. Lipson, "Ultra high bandwidth WDM using silicon microring modulators," *Optics Express*, vol. 18, no. 16, pp. 16 858–16 867, Aug/ 2010.

[26] Q. Xu, B. Schmidt, S. Pradhan, and M. Lipson, "Micrometre-scale silicon electro-optic modulator," *Nature*, vol. 435, pp. 325,327.

[27] P. Dong, C. Xie, L. L. Buhl, and Y.-K. Chen, "Silicon microring modulators for advanced modulation formats," in *Optical Fiber Communication Conference/National Fiber Optic Engineers Conference 2013*. Optical Society of America, 2013.

[28] K.-W. Ang, G.-Q. Lo, and D.-L. K. (2010), *Semiconductor Technologies*. InTech, 2010.

[29] J. J. Ackert, A. S. Karar, D. J. Paez, P. E. Jessop, J. C. Cartledge, and A. P. Knights, "10 Gbps silicon waveguide-integrated infrared avalanche photodiode," *Optics Express*, vol. 21, no. 17, pp. 19 530–19 537, Aug. 2013.

[30] A. Alduino, L. Liao, R. Jones, M. Morse, B. Kim, W.-Z. Lo, J. Basak, B. Koch, H.-F. Liu, H. Rong, M. Sysak, C. Krause, R. Saba, D. Lazar, L. Horwitz, R. Bar, S. Litski, A. Liu, K. Sullivan, O. Dosunmu, N. Na, T. Yin, F. Haubensack, I. wei Hsieh, J. Heck, R. Beatty, H. Park, J. Bovington, S. Lee, H. Nguyen, H. Au, K. Nguyen, P. Merani, M. Hakami, and M. Paniccia, "Demonstration of a high speed 4-channel integrated silicon photonics WDM link with hybrid silicon lasers," in *Integrated Photonics Research, Silicon and Nanophotonics and Photonics in Switching*. Optical Society of America, 2010.

[31] A. Narasimha, B. Analui, Y. Liang, T. J. Sleboda, S. Abdalla, E. Balmater, S. Gloeckner, D. Guckenberger, M. Harrison, R. G. M. P. Koumans, D. Kucharski, A. Mekis, S. Mirsaidi, D. Song, and T. Pinguet, "A fully integrated 4 x 10-gb/s DWDM optoelectronic transceiver implemented in a standard 0 13um cmos soi technology," *IEEE Journal of Solid-State Circuits*, vol. 42, no. 12, pp. 2736–2744, Dec. 2007.

[32] "Luxtera debuts 1310 nm 100G-PSM4 QSFP28, module and silicon photonics chipset at OFC 2015," Luxtera, Carlsbad, CA, Press Release, Mar. 2015.

[33] IBM announces silicon photonics breakthrough, set to break 100 Gb/s barrier. (Date Accessed: July 2016). [Online]. Available: http://www.extremetech.com/extreme/ 205713-ibm-announces-silicon-photonics-breakthrough-set-to-break-100gbs-barrier

[34] Skorpios technologies demonstrates 100G QSFP28 (100G-QSFP-CLR4). (Date Accessed:

July 2016). [Online]. Available: http://www.prnewswire.com/news-releases/skorpios-technologies-demonstrates-100g-qsfp28-100g-qsfp-clr4-249269151.html

[35] OFC2016: Inphi develops silicon photonics for data centers. (Date Accessed: July 2016). [Online]. Available: http://www.convergedigest.com/2016/03/ofc2016-inphi-develops-silicon.html

[36] Macom announces CWDM4 L-PIC for 100G datacenter applications. (Date Accessed: July 2016). [Online]. Available: http://www.convergedigest.com/2016/03/macom-announces-cwdm4-l-pic-for-100g.html

[37] "Quad small form- factor pluggable (QSFP) products," Tech. Rep., 2009.

[38] "CFP MSA CFP4 hardware specification," Tech. Rep., 2010, (Date Accessed: July 2016). [Online]. Available: http://www.cfp-msa.org/Documents/CFP-MSA-HW-Spec-rev1-40.pdf

[39] C. Cole, "100-Gb/s and beyond ethernet optical interfaces," Finisar Corporation, Tech. Rep.

[40] "Mellanox 100 Gb/s QSFP28 optical transceiver," Tech. Rep., 2016, (Date Accessed: August 2016). [Online]. Available: http://www.mellanox.com/related-docs/prod_cables/PB_100Gb_QSFP28_Transceiver.pdf

[41] R. Boeck, "High performance silicon photonic filters for dense wavelength-division multiplexing applications," Ph.D. dissertation, The University of British Columbia, April 2016.

[42] Y. A. Vlasov, "Silicon photonics for next generation computing systems," in *2008 34th European Conference on Optical Communication*, Sept. 2008, pp. 1–2, (Date Accessed: August 2016). [Online]. Available: http://researcher.ibm.com/researcher/files/us-yvlasov/vlasov%20ECOC%20tutorial%202008.pdf

[43] H. Jayatilleka, K. Murray, M. Caverley, N. A. F. Jaeger, L. Chrostowski, and S. Shekhar, "Crosstalk in soi microring resonator-based filters," *Journal of Lightwave Technology*, vol. 34, no. 12, pp. 2886–2896, June 2016.

[44] J. R. Ong, R. Kumar, and S. Mookherjea, "Ultra-high-contrast and tunable-bandwidth filter using cascaded high-order silicon microring

filters," *IEEE Photonics Technology Letters*, vol. 25, no. 16, pp. 1543–1546, Aug. 2013.

[45] F. Horst, W. M. J. Green, B. J. Offrein, and Y. A. Vlasov, "Silicon-on-insulator echelle grating WDM demultiplexers with two stigmatic points," *IEEE Photonics Technology Letters*, vol. 21, no. 23, pp. 1743–1745, Dec. 2009.

[46] M. R. Pearson, A. Bezinger, A. Delage, J. W. Fraser, S. Janz, P. E. Jessop, and D.-X. Xu, "Arrayed waveguide grating demultiplexers in silicon-on-insulator," pp. 11–18, Mar. 2000.

[47] F. Horst, W. M. Green, S. Assefa, S. M. Shank, Y. A. Vlasov, and B. J. Offrein, "Cascaded Mach-Zehnder wavelength filters in silicon photonics for low loss and flat pass-band WDM (de-)multiplexing," *Optics Express*, vol. 21, no. 10, pp. 11 652–11 658, May 2013.

[48] W. Shi, H. Yun, C. Lin, M. Greenberg, X. Wang, Y. Wang, S. T. Fard, J. Flueckiger, N. A. F. Jaeger, and L. Chrostowski, "Ultra-compact, flat-top demultiplexer using anti-reflection contra-directional couplers for CWDM networks on silicon," *Optics Express*, vol. 21, no. 6, pp. 6733–6738, Mar. 2013.

[49] S. Pathak, P. Dumon, D. V. Thourhout, and W. Bogaerts, "Comparison of awgs and echelle gratings for wavelength division multiplexing on silicon-on-insulator," *IEEE Photonics Journal*, vol. 6, no. 5, pp. 1–9, Oct. 2014.

[50] W. Shi, X. Wang, C. Lin, H. Yun, Y. Liu, T. Baehr-Jones, M. Hochberg, N. A. F. Jaeger, and L. Chrostowski, "Silicon photonic grating-assisted, contra-directional couplers," *Optics Express*, vol. 21, no. 3, pp. 3633–3650, Feb. 2013.

[51] K. Padmaraju, D. F. Logan, T. Shiraishi, J. J. Ackert, A. P. Knights, and K. Bergman, "Wavelength locking and thermally stabilizing microring resonators using dithering signals," *Journal of Lightwave Technology*, vol. 32, no. 3, pp. 505–512, Feb. 2014.

[52] R. Boeck, J. Flueckiger, H. Yun, L. Chrostowski, and N. A. F. Jaeger, "High performance vernier racetrack resonators," *Optics Letters*, vol. 37, no. 24, pp. 5199–5201, Dec. 2012.

[53] M. Watts, T. Barwicz, M. Popovic, P. Rakich, L. Socci, E. Ippen, H. I. Smith, and F. Kaertner, "Microring-resonator filter with doubled free-spectral-range by two-point coupling," in *Conference on Lasers and Electro-Optics*, vol. 1. Optical Society of America, May 2005, pp. 273–275.

[54] R. Boeck, J. Flueckiger, L. Chrostowski, and N. A. F. Jaeger, "Experimental performance of DWDM quadruple vernier racetrack resonators," *Optics Express*, vol. 21, no. 7, pp. 9103–9112, Apr. 2013.

[55] W. Shi, X. Wang, W. Zhang, H. Yun, C. Lin, L. Chrostowski, and N. A. F. Jaeger, "Grating-coupled silicon microring resonators," *Applied Physics Letters*, vol. 100, no. 12, 2012.

[56] R. Boeck, M. Caverley, L. Chrostowski, and N. A. F. Jaeger, "Silicon quadruple series-coupled vernier racetrack resonators: Experimental signal quality," in *Optical Fiber Communication Conference*. Optical Society of America, 2015, p. W2A.8.

[57] F. Morichetti, S. Grillanda, and A. Melloni, "Breakthroughs in photonics 2013: Toward feedback-controlled integrated photonics," *IEEE Photonics Journal*, vol. 6, no. 2, pp. 1–6, April 2014.

[58] M. S. Nawrocka, T. Liu, X. Wang, and R. R. Panepucci, "Tunable silicon microring resonator with wide free spectral range," *Applied Physics Letters*, vol. 89, no. 7, pp. –, 2006.

[59] A. Prabhu, A. Tsay, Z. Han, and V. Van, "Ultracompact soi microring add-drop filter with wide bandwidth and wide fsr," *IEEE Photonics Technology Letters*, vol. 21, no. 10, pp. 651–653, May 2009.

[60] S. Xiao, M. H. Khan, H. Shen, and M. Qi, "A highly compact third-order silicon microring add-drop filter with a very large free spectral range, a flat passband and a low delay dispersion," *Optics Express*, vol. 15, no. 22, pp. 14 765–14 771, Oct. 2007.

[61] G. Fan, R. Orbtchouk, B. Han, X. Liu, and Z. Zhen, "Improved coupling technique of ultracompact ring resonators in silicon-on-insulator technology," *Applied Optics*, vol. 51, no. 21, pp. 5212–5215, Jul. 2012.

[62] P. Chen, S. Chen, X. Guan, Y. Shi, and D. Dai, "High-order microring resonators with bent couplers for a box-like filter response," *Optics Letters*, vol. 39, no. 21, pp. 6304–6307, Nov. 2014.

[63] C. R. Doerr, M. Cappuzzo, E. Chen, A. Wong-Foy, L. Gomez, A. Griffin, and L. Buhl, "Bending of a planar lightwave circuit 2x2 coupler to desensitize it to wavelength, polarization, and fabrication changes," *IEEE Photonics Technology Letters*, vol. 17, no. 6, pp. 1211–1213, Jun. 2005.

[64] H. Morino, T. Maruyama, and K. Iiyama, "Reduction of wavelength dependence of coupling characteristics using si optical waveguide curved directional coupler," *Journal of Lightwave Technology*, vol. 32, no. 12, pp. 2188–2192, June 2014.

[65] D. Dai and J. E. Bowers, "Novel ultra-short and ultra-broadband polarization beam splitter based on a bent directional coupler," *Optics Express*, vol. 19, no. 19, pp. 18 614–18 620, Sep. 2011.

[66] J. Wang, D. Liang, Y. Tang, D. Dai, and J. E. Bowers, "Realization of an ultra-short silicon polarization beam splitter with an asymmetrical bent directional coupler," *Optics Letters*, vol. 38, no. 1, pp. 4–6, Jan. 2013.

[67] S. Chen, Y. Shi, S. He, and D. Dai, "Low-loss and broadband 2x2 silicon thermo-optic Mach-Zehnder switch with bent directional couplers," *Optics Letters*, vol. 41, no. 4, pp. 836–839, Feb. 2016.

[68] Y. Liu, R. Ding, Y. Ma, Y. Yang, Z. Xuan, Q. Li, A. E.-J. Lim, G.-Q. Lo, K. Bergman, T. Baehr-Jones, and M. Hochberg, "Silicon mod-MUX-ring transmitter with 4 channels at 40 Gb/s," *Optics. Express*, vol. 22, no. 13, pp. 16 431–16 438, Jun. 2014.

[69] M. Rakowski, M. Pantouvaki, P. D. Heyn, P. Verheyen, M. Ingels, H. Chen, J. D. Coster, G. Lepage, B. Snyder, K. D. Meyer, M. Steyaert, N. Pavarelli, J. S. Lee, P. O'Brien, P. Absil, and J. V. Campenhout, "22.5 a 4 x 20gb/s WDM ring-based hybrid CMOS silicon photonics transceiver," in *2015 IEEE International Solid-State Circuits Conference - (ISSCC) Digest of Technical Papers*, Feb 2015, pp. 1–3.

[70] X. Zheng, F. Liu, J. Lexau, D. Patil, G. Li, Y. Luo, H. Thacker, I. Shubin, J. Yao, K. Raj, R. Ho, J. E. Cunningham, and A. V. Krishnamoorthy,

"Ultra-low power arrayed CMOS silicon photonic transceivers for an 80 Gbps WDM optical link," in *Optical Fiber Communication Conference and Exposition (OFC/NFOEC), 2011 and the National Fiber Optic Engineers Conference*, Mar. 2011, pp. 1–3.

[71] C. H. Chen, C. Li, R. Bai, K. Yu, J. M. Fedeli, S. Meassoudene, M. Fournier, S. Menezo, P. Chiang, S. Palermo, M. Fiorentino, and R. Beausoleil, "DWDM silicon photonic transceivers for optical interconnect," in *2015 IEEE Optical Interconnects Conference (OI)*, April 2015, pp. 52–53.

[72] F. Xia, L. Sekaric, M. OBoyle, and Y. Vlasov, "Coupled resonator optical waveguides based on silicon-on-insulator photonic wires," *Applied Physics Letters*, vol. 89, no. 4, 2006.

[73] L. Chrostowski, S. Grist, J. Flueckiger, W. Shi, X. Wang, E. Ouellet, H. Yun, M. Webb, B. Nie, Z. Liang, K. C. Cheung, S. A. Schmidt, D. M. Ratner, and N. A. F. Jaeger, "Silicon photonic resonator sensors and devices," vol. 8236, 2012, pp. 823 620–823 620–16.

[74] O. Schwelb, "A decade of progress in microring and microdisk based photonic circuits: a personal selection," vol. 6872, 2008, pp. 68 720H–68 720H–14.

[75] W. Bogaerts, P. De Heyn, T. Van Vaerenbergh, K. De Vos, S. Kumar Selvaraja, T. Claes, P. Dumon, P. Bienstman, D. Van Thourhout, and R. Baets, "Silicon microring resonators," *Laser & Photonics Reviews*, vol. 6, no. 1, pp. 47–73, 2012.

[76] R. Boeck, L. Chrostowski, and N. A. F. Jaeger, "Sensitivity analysis of silicon-on-insulator quadruple vernier racetrack resonators," *Optical Engineering*, vol. 54, no. 11, p. 117102, 2015.

[77] Z. Lu, K. Murray, H. Jayatilleka, and L. Chrostowski, "Michelson interferometer thermo-optic switch on SOI with a 50 Mirowatt power consumption," *IEEE Photonics Technology Letters*, vol. 27, no. 22, pp. 2319–2322, Nov. 2015.

[78] W. R. McKinnon, D. X. Xu, C. Storey, E. Post, A. Densmore, A. Delâge, P. Waldron, J. H. Schmid, and S. Janz, "Extracting coupling and loss

coefficients from a ring resonator," *Opt. Express*, vol. 17, no. 21, pp. 18 971–18 982, Oct. 2009.

[79] P. Dong, W. Qian, H. Liang, R. Shafiiha, N.-N. Feng, D. Feng, X. Zheng, A. V. Krishnamoorthy, and M. Asghari, "Low power and compact reconfigurable multiplexing devices based on silicon microring resonators," *Optics Express*, vol. 18, no. 10, pp. 9852–9858, May 2010.

[80] P. Dong, W. Qian, H. Liang, R. Shafiiha, D. Feng, G. Li, J. E. Cunningham, A. V. Krishnamoorthy, and M. Asghari, "Thermally tunable silicon racetrack resonators with ultralow tuning power," *Optics Express*, vol. 18, no. 19, pp. 20 298–20 304, Sep. 2010.

[81] Z. Su, E. Timurdogan, J. Sun, M. Moresco, G. Leake, D. Coolbaugh, and M. Watts, "An interior-ridge silicon microring switch with integrated thermal tuner," in *Advanced Photonics*. Optical Society of America, 2015, p. IM2B.5.

[82] P. Orlandi, P. Velha, M. Gnan, P. Bassi, A. Samarelli, M. Sorel, M. J. Strain, and R. D. L. Rue, "Microring resonator with wavelength selective coupling in SOI," in *IEEE 8th International Conference on Group IV Photonics*. IEEE, Sept. 2011, pp. 281–283.

[83] R. Boeck, W. Shi, L. Chrostowski, and N. A. F. Jaeger, "FSR-eliminated Vernier racetrack resonators using grating-assisted couplers," *IEEE Photonics Journal*, vol. 5, no. 5, pp. 2 202 511–2 202 511, Oct. 2013.

[84] M. Caverley, R. Boeck, L. Chrostowski, and N. A. Jaeger, "High-speed data transmission through silicon contra-directional grating coupler optical add-drop multiplexers," in *2015 Conference on Laser and Electro-optics*. Optical Society of America, 2015, p. JTh2A.41.

[85] W. Shi, M. Greenberg, X. Wang, Y. Wang, C. Lin, N. A. F. Jaeger, and L. Chrostowski, "Single-band add-drop filters using anti-reflection, contra-directional couplers," in *The 9th International Conference on Group IV Photonics (GFP)*, Aug. 2012, pp. 21–23.

[86] P. Yeh and H. F. Taylor, "Contradirectional frequency-selective couplers for guided-wave optics," *Applied Optics*, vol. 19, no. 16, pp. 2848–2855, Aug. 1980.

[87] A. Yariv and P. Yeh, *Photonics: Optical Electronics in Modern Communications*, ser. The Oxford series in electrical and computer engineering. Oxford University Press, 2007, ch. 12.

[88] R. Boeck, M. Caverley, L. Chrostowski, and N. A. F. Jaeger, "Process calibration method for designing silicon-on-insulator contra-directional grating couplers," *Optics Express*, vol. 23, no. 8, pp. 10 573–10 588, Apr. 2015.

[89] J. Xie, L. Zhou, X. Sun, Z. Zou, L. Lu, H. Zhu, X. Li, and J. Chen, "Selective excitation of microring resonances using a pulley-coupling structure," *Applied Optics*, vol. 53, no. 5, pp. 878–884, Feb. 2014.

[90] R. Boeck, J. Flueckiger, L. Chrostowski, and N. A. F. Jaeger, "Experimental performance of DWDM quadruple Vernier racetrack resonators," *Optics Express*, vol. 21, no. 7, pp. 9103–9112, Apr. 2013.

[91] B. Kuo and F. Golnaraghi, *Automatic control systems*, ser. Automatic Control Systems. John Wiley & Sons, 2003, no. v. 1.

[92] R. J. Bojko, J. Li, L. He, T. Baehr-Jones, M. Hochberg, and Y. Aida, "Electron beam lithography writing strategies for low loss, high confinement silicon optical waveguides," *Journal of Vacuum Science & Technology B*, vol. 29, no. 6, 2011.

[93] Y. Wang, H. Yun, Z. Lu, R. Bojko, W. Shi, X. Wang, J. Flueckiger, F. Zhang, M. Caverley, N. A. F. Jaeger, and L. Chrostowski, "Apodized focusing fully etched subwavelength grating couplers," *IEEE Photonics Journal*, vol. 7, no. 3, pp. 1–10, June 2015.

[94] A. Melloni, M. Martinelli, G. Cusmai, and R. Siano, "Experimental evaluation of ring resonator filters impact on the bit error rate in non return to zero transmission systems," *Optics Communications*, vol. 234, no. 16, pp. 211 – 216, 2004.

[95] R. Boeck, M. Caverley, L. Chrostowski, and N. A. F. Jaeger, "Silicon quadruple series-coupled Vernier racetrack resonators: Experimental signal quality," in *Optical Fiber Communication Conference*. Optical Society of America, 2015, p. W2A.8.